Visualizing functional human profilin in cells and in vitro applications

Morgan L. Pimm[1], Xinbei Liu[1], Farzana Tuli[1], Ashley Lojko[1], and Jessica L. Henty-Ridilla ✉[1,2]

[1]Department of Biochemistry and Molecular Biology, SUNY Upstate Medical University, Syracuse, NY, 13210, USA.
[2]Department of Neuroscience and Physiology, SUNY Upstate Medical University, Syracuse, NY, 13210, USA.

Profilin is an essential regulator of actin and microtubule dynamics and therefore a critical control point for the normal division, motility, and morphology of cells. Most studies of profilin have focused on biochemical investigations using purified protein because high cellular concentrations present challenges for conventional imaging modalities. In addition, past studies that employed direct labeling or conventional fusion protein strategies compromised different facets of profilin function. We engineered two versions of tagged profilin that retain native activities with respect to phosphoinositide lipids, actin monomers, formin-mediated actin assembly, and microtubule polymerization. mApple-profilin-1 directly binds to dimers of tubulin (k_D = 1.7 µM) and the microtubule lattice (k_D = 10 µM) to stimulate microtubule assembly. In cells, Halo-tagged profilin-1 fully rescues profilin-1$^{(-/-)}$ cells from knockout-induced perturbations to cell shape, actin filament architecture, and microtubule arrays. In cells expressing Halo-profilin, we visualized a subset of individual molecules of profilin-1 by titrating fluorescent Halo-ligands. Further, we combined this imaging approach with specific function-disrupting point-mutants in profilin to visualize dynamic profilin associated with microtubules in live-cells. Thus, these tagged profilins are reliable tools for studying the dynamic interactions of profilin with actin or microtubules in live-cell or in vitro applications.

profilin | actin | microtubules | tubulin | formin | PIP-lipids
Correspondence: ***ridillaj@upstate.edu***

Introduction

Profilin is a small (~15 kDa) cytosolic protein with binding regions required for interacting with phosphoinositide (PIP) lipids, actin monomers, poly-L-proline (PLP) containing ligands, and microtubules. Through these interactions, it plays critical roles in signal transduction cascades, apoptosis, motility, phagocytosis, and mitosis (Davey and Moens, 2020; Pimm et al., 2020; Karlsson and Dráber, 2021). Profilin is a classic regulator of actin dynamics that directly binds actin monomers to suppress actin filament assembly. Interactions between profilin and PIP lipids further fine tune actin assembly in cell signaling cascades (Lassing and Lindberg, 1985; Krishnan and Moens, 2009; Ding et al., 2012; Davey and Moens, 2020). In contrast to these mechanisms, profilin stimulates actin polymerization through interactions mediated by poly-L-proline (PLP) tracts in key regulators like formins or Ena/VASP. Combined, these activities effectively regulate many properties of the actin monomer pool and bias actin polymerization in favor of straight filament architectures (Henty-Ridilla and Goode, 2015; Rotty et al., 2015; Suarez et al., 2015; Suarez and Kovar, 2016; Skruber et al., 2018). Despite similar concentrations, not all cellular profilin is bound to actin monomers (Goldschmidt-Clermont et al., 1992; Kaiser et al., 1999; Skruber et al., 2018, 2020; Zweifel and Courtemanche, 2020). Some profilin outcompetes actin bound to intracellular lipids present on membranes and vesicles to transmit distinct cellular signals (Lassing and Lindberg, 1985; Davey and Moens, 2020). Profilin also directly regulates cellular microtubule dynamics and organization (Witke et al., 1998; Nejedla et al., 2016; Henty-Ridilla et al., 2017; Pinto-Costa and Sousa, 2019; Pimm et al., 2020; Karlsson and Dráber, 2021; Nejedlá et al., 2021; Pimm and Henty-Ridilla, 2021). Despite the importance in regulating these essential activities, existing profilin probes compromise different facets of function. Consequently, most of what is known about profilin has been ascertained outside of the cell, determined from in vitro biochemical assays.

Conventional protein tagging strategies compromise profilin functions (Skruber et al., 2018; Pimm et al., 2020). To complicate matters further, because profilin is present at high cellular concentrations (8-500 µM, depending on the cell type), fluorescent probes often oversaturate signals collected from conventional imaging modalities (Wittenmayer et al., 2000; Henty-Ridilla et al., 2017; Nejedla et al., 2017; Funk et al., 2019; Nejedlá et al., 2021). Direct (cysteine/maleimide) labeling approaches for detecting individual molecules of protein require 4-5 amino acid modifications in profilin. Each of these substitutions results in aggregation and compromised function in human profilin (Vidali and Hepler, 1997; Vinson et al., 1998; Kaiser et al., 1999; Henty-Ridilla et al., 2017). Microinjection experiments require advanced imaging tools, skills, and directly labeled profilin, but can be performed in live-cells without overexpression. While this technique is challenging to perform, it is able to localize profilin to sites of actin assembly, lipid membranes, and the nucleus (Lassing and Lindberg, 1985; Hartwig et al., 1989; Tarachandani and Wang, 1996; Kaiser et al., 1999; Zhu et al., 2021). Positioning a GFP-derived fluorescent tag on the C- or N-terminus disrupts PLP- and PIP-binding interactions, effectively rendering the fluorescent version flawed for critical measurements in cells (Wittenmayer et al., 2000; Antoine et al., 2020). Splitting profilin by inserting a fluorescent tag in a protruding loop in the center of the protein retains normal binding affinity for PLP and lipids, but compromises actin functions (Nejedla et al., 2017; Karlsson and Dráber, 2021; Nejedlá et al., 2021). Further, this approach of splitting pro-

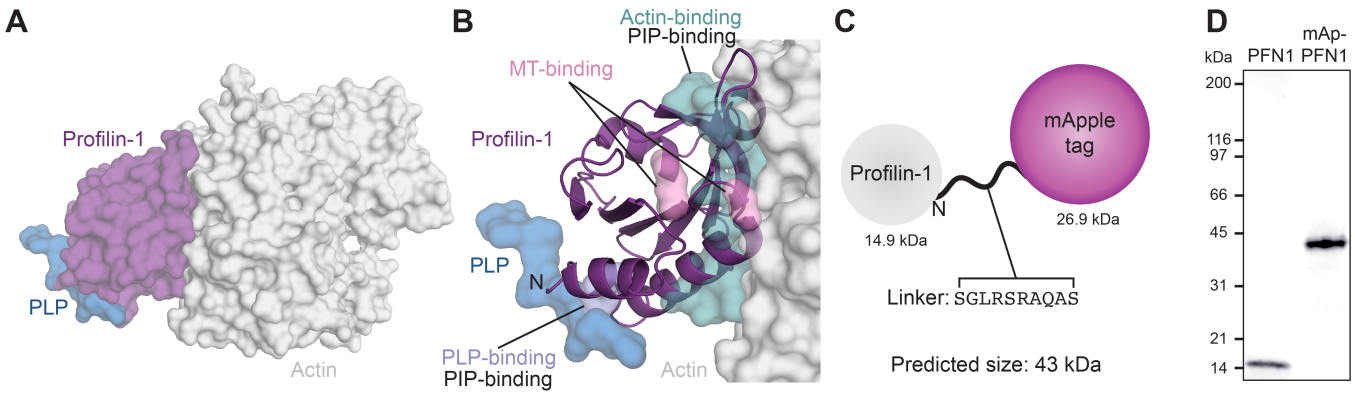

Fig. 1. Strategy for fluorescently tagging and purifying profilin-1. (A) View of profilin (purple) interacting with actin (gray) and the poly-L-proline (PLP) region of VASP (blue), modeled using PDB: 2BTF (Schutt et al., 1993) and PDB: 2PAV (Ferron et al., 2007). **(B)** Magnified view showing profilin surfaces in contact with actin and PLP. The positions of key residues are highlighted as follows: actin-binding residues (teal), PLP-binding (Y6D; light blue), and microtubule binding (M114, G118; pink). **(C)** Design of tagged-profilin-1 fusion protein. The tag (mApple or Halo) was positioned at the N-terminus of Human profilin-1 following a ten amino acid linker sequence (SGLRSRAQAS). **(D)** Coomassie-stained SDS-PAGE gel of profilin (PFN1) and mApple-profilin-1 (mAp-PFN1) expressed and purified from bacterial lysates.

filin with a genetically encoded fluorescent protein cannot be universally applied to all profilins (i.e., different species or isoforms).

A popular imaging approach to circumvent some of these issues employs anti-profilin antibodies to stain detergent-extracted remnants of fixed cells (Henty-Ridilla et al., 2017; Nejedla et al., 2017; DeCaprio and Kohl, 2020; Nejedlá et al., 2021). This technique unambiguously localizes profilin to stable cytoskeletal structures (i.e., stress fibers, the sides of microtubules, nuclear components) in cells. However, it obscures the fine spatiotemporal details required to measure the flux or dynamics of cellular pools of profilin. To date >10 different engineered profilins have been produced, yet no uniform tagging strategy is able to retain native profilin functions or can be applied across species, with different isoforms, or in varying cellular situations. Here, we engineered and characterized two new versions of tagged profilin that behave identically to the untagged native protein. We overcome the drawbacks of previous approaches using a flexible linker at the N-terminus coupled with GFP-derived or titratable self-labeling approaches (i.e., SNAP-, Halo-, or CLIP-tags). Tagged profilin binds PIP lipids, actin monomers, PLP-containing ligands, and microtubules. In cells, tagged profilin fully rescues knockout-induced perturbations to cell shape, actin filament architecture, and microtubule arrays. Further, titrations of fluorescent ligands to visualize Halo-profilin permit the detection of single-molecules of profilin in cells, both in the cytoplasm and associated with microtubules. The tagging strategy used here applies across cell types and isoforms and permits the study of profilin in cellular homeostasis, disease states, and in vitro biochemical applications.

Results

Design of tagged profilin.

Tagging human profilin without compromising its canonical activities has been extremely challenging. Profilin is considerably smaller than conventional genetically encoded fluorescent tags (profilin is ~15 kDa whereas GFP is ~27 kDa). Traditional direct labeling approaches are cytotoxic and disrupt actin-based functions (Wittenmayer et al., 2000; Henty-Ridilla et al., 2017; Skruber et al., 2018; Pimm et al., 2020). Critical aspects of profilin's function occur through conserved binding sites for PIP lipids, actin monomers, poly-L-proline (PLP) motifs, or microtubules (Figures 1A and 1B). Estimates of cellular profilin concentration in mammalian cells are very high (>10 μM) depending on the specific cell type (Koestler et al., 2009; Funk et al., 2019), presenting challenges to localizing fluorescent probes or antibodies. To directly monitor profilin activities, we engineered two versions of human profilin-1 visible with either an mApple fluorescent probe or through fluorescent ligands that bind to a Halo-tagged version (Figure 1C). We cloned mApple- or Halo-tags fused to a ten amino acid flexible linker on the N-terminus of human profilin-1. We chose the mApple fluorescent probe because it is a bright and relatively stable protein that avoids overlap with the excitation and emission ranges of well characterized actin-labels used in biochemical assays (i.e. Oregon-Green and pyrene-labeled actin) (Shaner et al., 2008; Bindels et al., 2017). The ten amino acid linker composition was chosen for flexibility and overall protein stability based on previous cDNA constructs from the Michael Davidson Fluorescent Protein Collection (https://www.addgene.org/fluorescent-proteins/davidson/). We expressed and purified recombinant versions of untagged or mApple-profilin to compare the effects of tagged profilin in several in vitro biochemistry assays. SDS-PAGE analysis revealed that the untagged and tagged versions of profilin were the expected size and highly pure (Figure 1D).

mApple-profilin binds phosphoinositide lipids with similar affinity as untagged profilin.

All profilins are known to bind some form of phosphoinositide lipid alone, or in complex with actin monomers. Association between lipids and profilin occurs through two different binding surfaces on profilin, overlapping with either the actin- or PLP-binding residues (Figure 1B) (Hartwig et al., 1989; Goldschmidt-Clermont et al., 1990;

Lambrechts et al., 2002; Skare and Karlsson, 2002; Ferron et al., 2007; Nejedla et al., 2017). While there are many versions of phosphatidyl inositol phosphate (PIP) signaling lipids, PI(4,5)P_2 is the best-characterized regulator of actin organization (Davey and Moens, 2020). At the plasma membrane, PI(4,5)P_2 directly interacts with profilin to inhibit actin dynamics and regulate overall cell morphology (Niggli, 2005). Profilin also binds PI(3,5)P_2, which regulates late endosomal trafficking to the lysosome (Goldschmidt-Clermont et al., 1990; Martys et al., 1996; Dong et al., 2000; Hong et al., 2015; De Craene et al., 2017; Hasegawa et al., 2017; Wallroth and Haucke, 2018; Lees et al., 2020). We performed liposome pelleting assays for PI(3,5)P_2 or PI(4,5)P_2 (Figure 2A) (Banerjee and Kane, 2017; Chandra et al., 2019). We detected mApple-profilin bound to either PI(3,5)P_2- or PI(4,5)P_2-containing liposomes via western blots using profilin-specific antibodies. Untagged profilin did not pellet in buffer controls lacking liposomes. Antibodies detected profilin-1 in the liposome pellet of control reactions containing phosphatidylserine or reactions containing either PI(3,5)P_2 or PI(4,5)P_2 lipids (Figures 2B and 2D). Similar to untagged profilin, mApple-profilin was only detected in reactions containing PIP lipids (Figures 2C and 2D). Quantitative comparisons subtracting the amount of profilin-bound non-specifically to liposome controls, demonstrate that mApple-profilin binds either PI(3,5)P_2 or PI(4,5)P_2 with similar affinity to untagged profilin. (Figures 2D and 2E). Thus, mApple-tagged profilin retains functional interactions with two important PIP lipids.

Direct visualization of fluorescent-profilin with polymerizing actin filaments.

Profilin binds to actin monomers as a 1:1 complex that strongly suppresses actin nucleation or minus-end monomer addition through steric hinderance interactions (Blanchoin et al., 2014). However, profilin binding interactions are typically indirectly assessed, recorded as reduced total actin polymerization in bulk assays, or reduced actin filament nucleation rates in microscopy-based assays that monitor actin polymerization. To date, the most reliable approach for measuring direct binding between profilin and actin monomers is isothermal titration calorimetry (ITC) (k_D = 0.1 μM (Wen et al., 2008). However, the major limitation to this approach is the requirement of copious amounts of protein for measurements. We used fluorescence anisotropy to measure the binding affinity between untagged profilin and Oregon-Green (OG)-labeled monomeric actin (Figure S2). We were unable to detect a change in anisotropy at any concentration of profilin used, consistent with previous reports (Vinson et al., 1998; Kaiser et al., 1999). Several studies demonstrate that thymosin β4 (Tβ4) competes with profilin to bind unlabeled actin monomers (Goldschmidt-Clermont et al., 1992; Aguda et al., 2006; Xue et al., 2014). First, we confirmed the binding affinity of GFP-Tβ4 for unlabeled actin monomers using fluorescence anisotropy (k_D = 5.4 ± 6.7 nM) (Figure 3A). We next performed competitive fluorescence anisotropy assays in the presence of GFP-Tβ4 to determine the affinity of actin monomers for either profilin protein (untagged or mApple-tagged) (Figure 3B). Untagged (k_D = 99.3 ± 12.4 nM) and fluorescently-tagged profilin (k_D = 96.3 ± 23.4 nM) bound actin monomers with affinities that were not statistically different (Figure 3B). We also confirmed the affinity of mApple-profilin and unlabeled actin monomers in the absence of GFP-Tβ4 (i.e., non-competitive assay). Fluorescent profilin directly bound actin monomers with a similar affinity (k_D = 105.2 ± 26.9 nM) (Figure 3C). Thus, mApple-profilin binds actin monomers with untagged, wild-type affinity.

We next compared the rates of actin assembly in the presence of untagged or mApple-profilin in bulk actin-fluorescence assays (Figure 3D). Compared to the actin alone control, less total actin polymer was made in the presence of profilin (Figure 3D). Actin filaments in the presence of mApple-profilin polymerized to similar levels as with untagged profilin and less efficiently than the actin alone control. This demonstrates that both versions of profilin inhibit the spontaneous nucleation of actin filaments. To investigate this further, we used single-molecule total internal reflection fluorescence (TIRF) microscopy to directly visualize actin assembly in the presence of our various versions of profilin (Figure 3E). TIRF reactions containing untagged profilin or mApple-profilin had similar levels of OG-actin fluorescence and less total fluorescence than actin alone controls (Figure 3E). To better understand the effects of mApple-profilin on actin assembly, we examined the nucleation and elongation phases of actin filament formation. We measured an average of 45.3 ± 1.4 filaments per field of view (FOV), in control assays where actin filaments were assembled alone (Figure 3F). We measured significantly fewer actin filaments in reactions supplemented with either untagged (21.5 ± 3.4) or mApple-profilin (19.8 ± 2.9) compared to actin alone controls (Figure 3F). The mean rate of actin filament polymerization in the presence of mApple-profilin was 10.05 ± 0.16 subunits s^{-1} μM^{-1} and is not significantly different than the untagged version measured as 10.07 ± 0.16 subunits s^{-1} μM^{-1} (Figure 3G). Neither of these rates differs significantly from the rate of free barbed-end growth obtained from reactions containing actin alone (10.07 ± 0.16 subunits s^{-1} μM^{-1}). In sum, mApple-profilin binds actin monomers, inhibits actin filament nucleation, and does not alter the rate of actin filament elongation. Each of these activities is indistinguishable from untagged profilin.

Profilin has strikingly different affinities for actin monomers (k_D = 100 nM) and for the growing ends of actin filaments (k_D = 225 μM) (Courtemanche and Pollard, 2013; Pernier et al., 2016; Funk et al., 2019; Pimm et al., 2020; Zweifel and Courtemanche, 2020). This property permits the effective disassociation of profilin from the ends of growing actin filaments during polymerization (Courtemanche and Pollard, 2013; Pernier et al., 2016; Zweifel and Courtemanche, 2020). Many of the actin-assembly roles of profilin revolve around its ability to bind actin monomers. However at high stochiometric concentrations, profilin binds actin filaments and may interfere with actin elongation (Jégou et al., 2011; Courte-

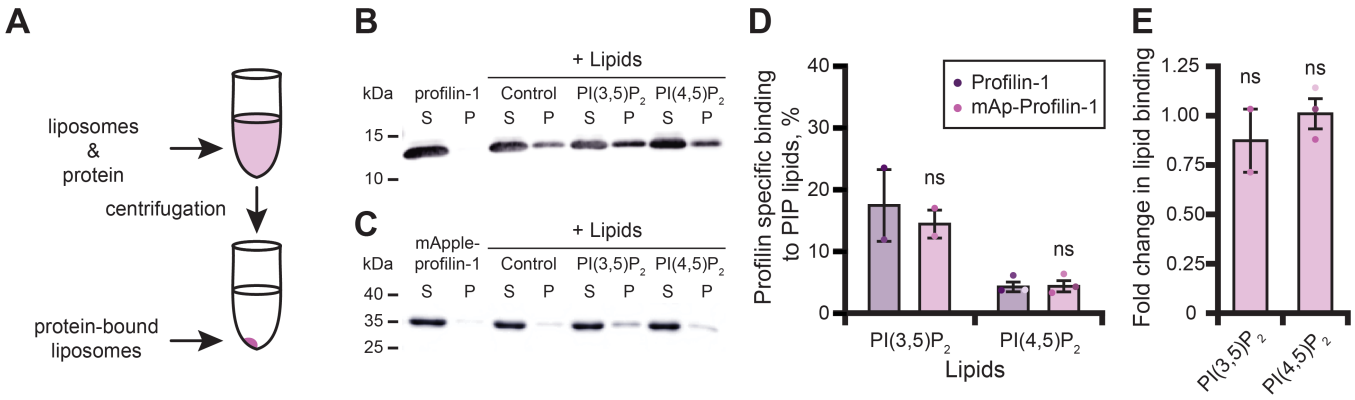

Fig. 2. Tagged profilin binds phosphoinositide (PIP)-lipids. (A) Schematic detailing liposome pelleting assays used to determine the binding efficiency of profilin proteins for phosphatidylinositol 3,5-bisphoshate (PI(3,5)P_2) or phosphatidylinositol 4,5-bisphoshate (PI(4,5)P_2) lipids. **(B)** Representative western blot of supernatants and pellets from liposome pelleting assays containing 1 µM profilin in absence (control) or presence of 0.33 mM of either PIP-lipid. Profilin-1 B 10 was used as a primary antibody (1:5,000 dilution; SantaCruz 137235) and goat anti-mouse 926-32210 was used as the secondary antibody (1:10,000 dilution; LiCor Biosciences). **(C)** Representative western blot of supernatants and pellets from liposome pelleting assays as in (B) for mApple-profilin. Bands for mApple-profilin binding appear lighter than untagged profilin pelleting in (B) because background binding to control lipids was subtracted from PIP-lipid binding for each profilin. **(D)** Band intensities from western blots in (B and C) were quantified to determine the amount of profilin-specific binding to PI(3,5)P_2 or PI(4,5)P_2. **(E)** The fold change in lipid binding of mApple-profilin compared to the untagged version. The affinity of tagged profilin for either lipid was not significantly different from the untagged version. Shaded values in (D) and (E) represent the individual data points used to determine the mean from (n = 2-3) independent experiments. Error bars indicate standard error. Significant differences were determined by Student's t-test. ns, not significantly different from control. Images of full blots are presented in Figure S1.

manche and Pollard, 2013; Funk et al., 2019; Zweifel and Courtemanche, 2020). We performed two-color TIRF microscopy to visualize the localization of mApple-profilin with polymerizing actin filaments (Figure S3A). The majority of polymerizing actin filaments visualized did not appear to have mApple-profilin associated with growing filament ends or sides (Figure S3A). One actin filament appeared to have a single-molecule of mApple-profilin associated with the growing end (Figure S3B). This single event was extremely transient and lasted for <5 s (Figures S3B and S3C). Further associations may occur on timescales and resolutions unable to be resolved with our imaging system or at concentrations closer to the predicted constant required for barbed-end association (K_D > 20 µM) (Jégou et al., 2011; Courtemanche and Pollard, 2013; Pernier et al., 2016; Funk et al., 2019; Skruber et al., 2020). Higher concentrations of fluorescent profilin may also conceal the dynamics of individual profilin molecules due to higher background fluorescence levels. These data suggest that most mApple-profilin in these assays is associated with the actin monomer pool rather than localized to actin filaments.

Fluorescent profilin stimulates formin-based actin filament assembly.

In addition to its role as a strong inhibitor of actin filament assembly (Figure 3), profilin can simultaneously bind actin monomers and proline-rich motifs (i.e., PLP) present in cytoskeletal regulatory proteins that include: formins, Ena/VASP, and WASP/VCA-domain containing proteins that activate the Arp2/3 Complex (Reinhard et al., 1995; Gertler et al., 1996; Chang et al., 1997; Evangelista, 1997; Mammoto et al., 1998; Miki et al., 1998; Suetsugu et al., 1998; Higgs and Pollard, 1999; Evangelista et al., 2002; Rodal et al., 2003; Ferron et al., 2007). The competition for profilin-actin between different actin nucleation systems has led to the popular idea that profilin tunes specific forms of actin assembly (branched or straight filaments) depending on the concentration of active nucleation proteins present (Rotty et al., 2015; Suarez et al., 2015; Skruber et al., 2018, 2020). Therefore, we tested whether mApple-profilin was capable of actin filament assembly through the PLP motif-containing formin, mDia1. Actin filaments assembled to similar levels in bulk pyrene fluorescence assays containing actin monomers and either untagged or mApple-profilin, (Figure 4A). The addition of a constitutively active formin, mDia1(FH1-C), to these reactions resulted in strongly enhanced actin polymerization compared to reactions lacking profilin (Figure 4A). Thus, mApple-profilin stimulates formin-based actin assembly indistinguishable from native profilin.

To investigate this hypothesis further, we used TIRF microscopy to directly visualize actin assembly in the presence of mDia1(FH1-C) and either profilin protein (Figures 4B and S4A). TIRF reactions of untagged profilin or mApple-profilin had significantly more OG-actin fluorescence compared to reactions without formin (Figure 4C). As a readout of actin filament nucleation, we counted the number of actin filaments from TIRF movies in the presence of formin (Figure 4D). We counted an average of 659.3 ± 98.3 filaments from TIRF reactions containing actin and mDia1(FH1-C), which was significantly higher (p = 0.014, ANOVA) than reactions containing actin alone or either actin-profilin or actin-mApple-profilin controls. Reactions containing formin and either untagged (42.7 ± 9.8 filaments) or mApple-profilin (48.3 ± 14.5 filaments) had statistically fewer filaments than control reactions assessing the combination of formin and actin (p = 0.0004, ANOVA), consistent with previous reports that profilin also suppresses formin nucleation (Kovar et al., 2006; Zweifel and Courtemanche, 2020). Thus, on its own, mApple-profilin inhibits actin polymerization (Figure 3). In

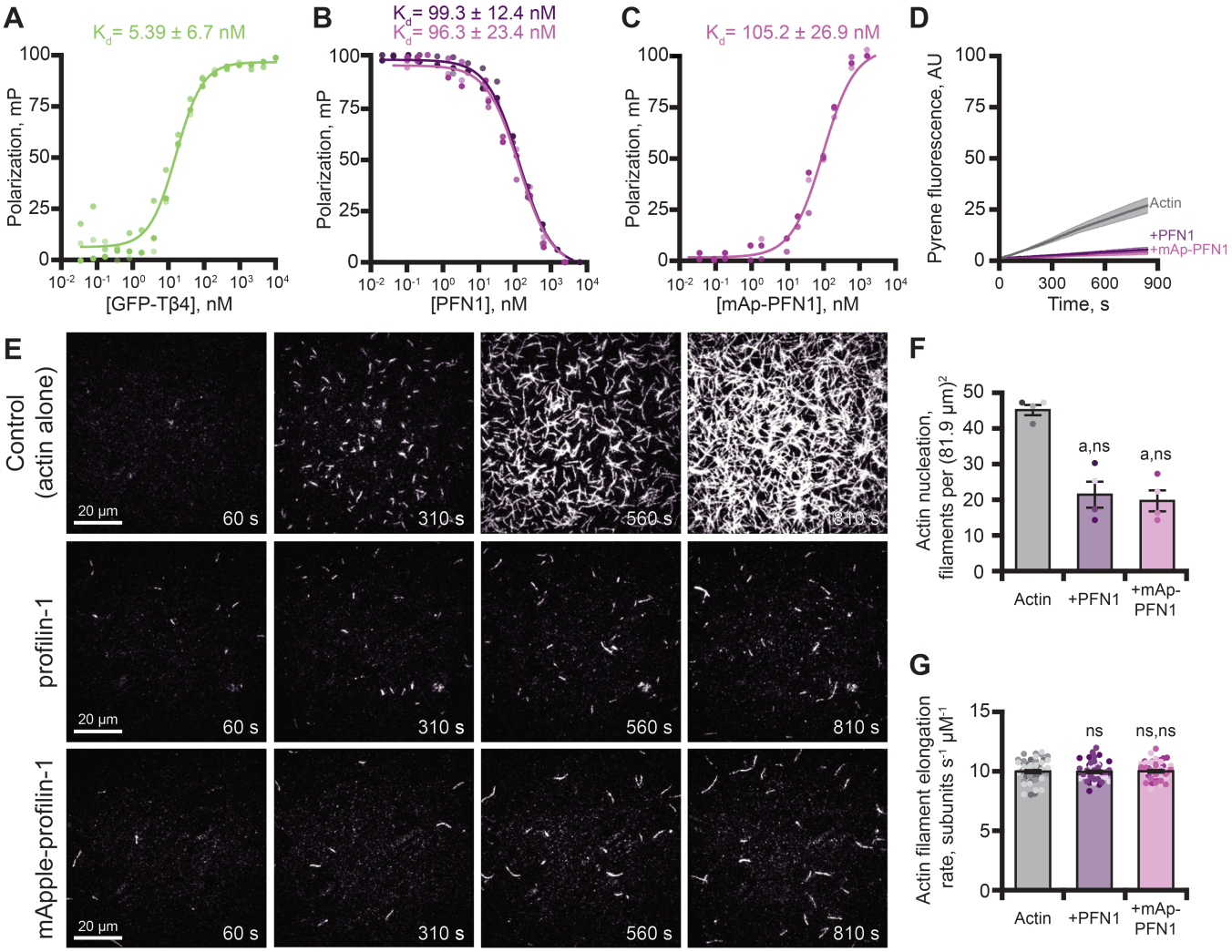

Fig. 3. Tagged profilin binds actin monomers with affinity equivalent to native profilin. (A) Fluorescence anisotropy of 10 nM actin (unlabled) mixed with increasing concentrations of GFP-thymosin β4 (GFP-Tβ4). **(B)** Competitive fluorescence anisotropy measurement of 10 nM GFP-Tβ4, 10 nM unlabeled actin monomers, and increasing concentrations of profilin (purple) or mApple-profilin (pink). **(C)** Fluorescence anisotropy measurement of 10 nM unlabeled actin and increasing concentrations of mApple-profilin. **(D)** Bulk fluorescence comparing the rate of actin assembly with either profilin protein. Reactions contain: 2 µM actin (5% pyrene-labeled), and 3 µM profilin (PFN1) or 3 µM mApple-profilin (mAp-PFN1). Shaded values represent SEM from three independent trials. **(E)** Time lapse images from TIRF microscopy assays monitoring the assembly of 1 µM actin (20% Oregon Green (OG)-labeled, 0.6 nM biotin-actin) in the presence or absence of 3 µM profilin or 3 µM mApple-profilin. Scale bar, 20 µm. See Supplemental Movies 1 and 2. **(F)** Average number of filaments visible after 100 s of actin assembly, visualized as in (E). Data were quantified from four separate reactions (FOV) from four independent reactions. **(G)** Distribution of actin filament elongation rates from TIRF reactions as in (E) (n = 51 filaments per condition). Shaded values in (A-C) and (F-G) represent the individual data points used to determine the mean from (n = 4) independent experiments. Error bars indicate SE based on the means of technical replicates. Significant differences by one-way ANOVA with Bartlett's correction for variance: ns, not significantly different from 1 µM actin alone control; a, compared with control ($p < 0.05$). The second ns refers to the comparison between untagged profilin and mApple-profilin.

contrast, in the presence of formin (mDia1), mApple-profilin stimulates actin filament assembly in a manner similar to the untagged protein.

We next explored whether mApple-profilin was capable of accelerating the rate of formin-mediated actin filament elongation in TIRF microscopy assays (Figure 4E). In these reactions we measured actin filaments elongating at two different speeds. The slowest speed corresponded to the rate of actin assembly with a free barbed end (~10 subunits s^{-1} μM^{-1}) (Kovar et al., 2006; Henty-Ridilla et al., 2016). The faster speed corresponded to the previously recorded rate of mDia1(FH1-C)-mediated actin filament assembly (~50 subunits s^{-1} μM^{-1}) (Kovar et al., 2006; Henty-Ridilla et al., 2016). The accelerated rate of actin filament assembly was exclusively observed in reactions that contained actin, mDia1(FH1-C), and untagged profilin (42.7 ± 9.8 subunits s^{-1} μM^{-1}) or mApple-profilin (48.3 ± 14.5 subunits s^{-1} μM^{-1}). We also used two-color TIRF assays to investigate the localization of mApple-profilin on actin filaments in the presence of formin. We did not notice a strong association of mApple-profilin with actin filaments containing formin (Figure S4B). However, the acquisition time used for these experiments (5 s intervals) does not exclude this possibility. Thus, these results demonstrate that both version of profilin (untagged or mApple-profilin) stimulate the nucleation and elongation phases of formin-based actin assembly at comparable levels.

Profilin directly binds tubulin dimers and enhances the growth rate of microtubules in vitro.

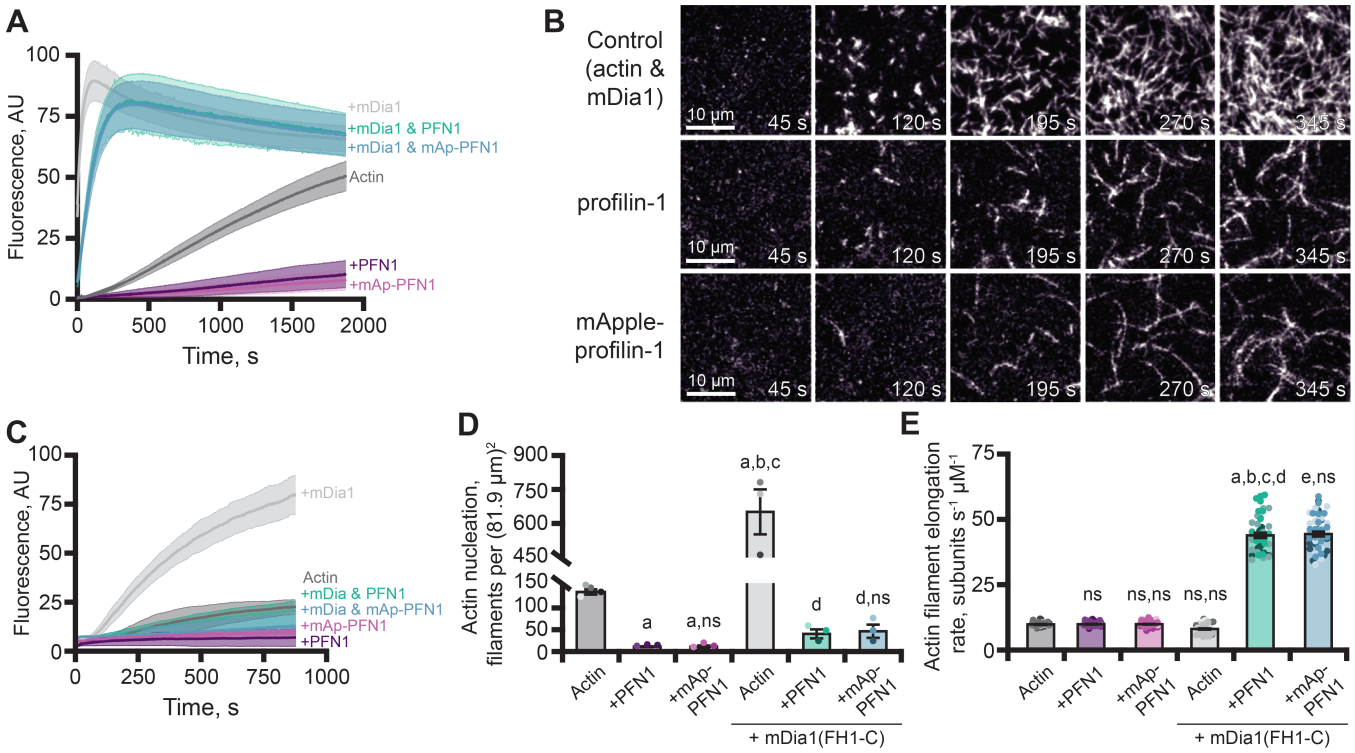

Fig. 4. Effects of tagged profilin on formin-mediated actin assembly. (A) Bulk pyrene fluorescence comparing the rate of formin-mediated actin assembly in the presence or absence of different profilins. Reactions contain: 2 µM actin (5% pyrene-labeled), 25 nM mDia1(FH1-C), and 5 µM profilin (PFN1) or 5 µM mApple-profilin (mAp-PFN1). Shaded values represent SEM from three independent trials. **(B)** Representative images from time lapse TIRF experiments. Reactions contain: 1 µM actin (10% Alexa-647-labeled, 0.6 nM biotin-actin), 25 nM mDia1(FH1-C), and 5 µM profilin (PFN1) or 5 µM mApple-profilin (mAp-PFN1). Scale bar, 10 µm. See Supplemental Movies 3 and 4. **(C)** Graph of total actin polymer mass over time, averaged from the fluorescence intensity of multiple fields of view (FOV) from TIRF reactions. Shading indicates SE for each condition. **(D)** Average number of filaments visible after 100 s of actin assembly, visualized as in (B). **(E)** Actin filament elongation rates from TIRF reactions as in (B) (n = 51 filaments per condition). Shaded values in (D-E) represent the individual data points used to determine the mean from at least three independent experiments. Error bars indicate SE. Significant differences by one-way ANOVA with Bartlett's correction for variance: ns, not significantly different from the actin alone control; a, compared with control ($p < 0.05$); b, compared with untagged profilin ($p < 0.05$); c, compared with mApple-profilin (mAp-PFN1) ($p < 0.05$); d, compared with actin and mDia1(FH1-C) control ($p < 0.05$); e, significantly different from all conditions except actin, mDia1(FH1-C) and untagged profilin ($p < 0.05$).

In addition to its well-established roles regulating actin polymerization, profilin influences microtubule polymerization through direct and indirect mechanisms. We used TIRF microscopy to compare microtubule dynamics in the presence and absence of untagged profilin or mApple-profilin (Figure 5A). In all reactions, microtubules displayed instances of dynamic instability, stochastically switching between periods of growth and shortening. Fluorescent microtubules in reactions containing free tubulin dimers and profilin grew at a rate ~6-fold faster than tubulin alone controls, from 1.9 ± 0.2 μm^{-1} min^{-1} to 12.7 ± 0.3 μm^{-1} min^{-1} (Figures 5B and 5C) (Henty-Ridilla et al., 2017). Microtubules in experiments including mApple-profilin elongated at significantly accelerated rates (12.6 ± 0.4 μm^{-1} min^{-1}) compared to controls ($p < 0.0001$, ANOVA). Consistent with an accelerated microtubule growth rate, the mean length of microtubules in reactions containing either profilin protein was significantly longer (Figure 5D; $p < 0.0001$, ANOVA). Microtubules polymerized in the presence of untagged or mApple-profilin were also more stable (Figure 5E). Specifically, the microtubule stability index (ratio of rescue to catastrophe events) was increased in favor of more steadily growing microtubules ($p < 0.0001$, ANOVA).

Previous observations suggest that profilin increases the on rate of tubulin at microtubule ends to facilitate microtubule elongation (Henty-Ridilla et al., 2017). Consistent with this hypothesis, microtubules were observed in TIRF reactions performed at concentrations of free tubulin below the critical concentration required for microtubule assembly (Henty-Ridilla et al., 2017). While our experiments were performed above the critical concentration for microtubule assembly, we observed a comparable and significant increase in the mean number of microtubules present in FOVs from TIRF assays performed in the presence of either profilin protein (Figure 5F) ($p = 0.0048$, ANOVA). The effects of profilin on microtubule polymerization could be explained by a number of possible mechanisms, including that profilin binds or stabilizes tubulin dimers at growing microtubule ends. To test this hypothesis, we performed fluorescence anisotropy to test for a direct interaction between mApple-profilin and unlabeled tubulin dimers. Fluorescent profilin indeed directly bound to tubulin dimers (k_D = 1.7 ± 2.0 µM) (Figure 5G). This binding constant, in the micromolar range, is much less than the physiological concentration of profilin or tubulin. Furthermore, profilin binds the sides of microtubules with much lower affinity (k_D = ~10 µM; Henty-Ridilla et al., 2017). This result supports the idea that profilin-enhanced microtubule polymerization occurs by orienting or stabilizing tubu-

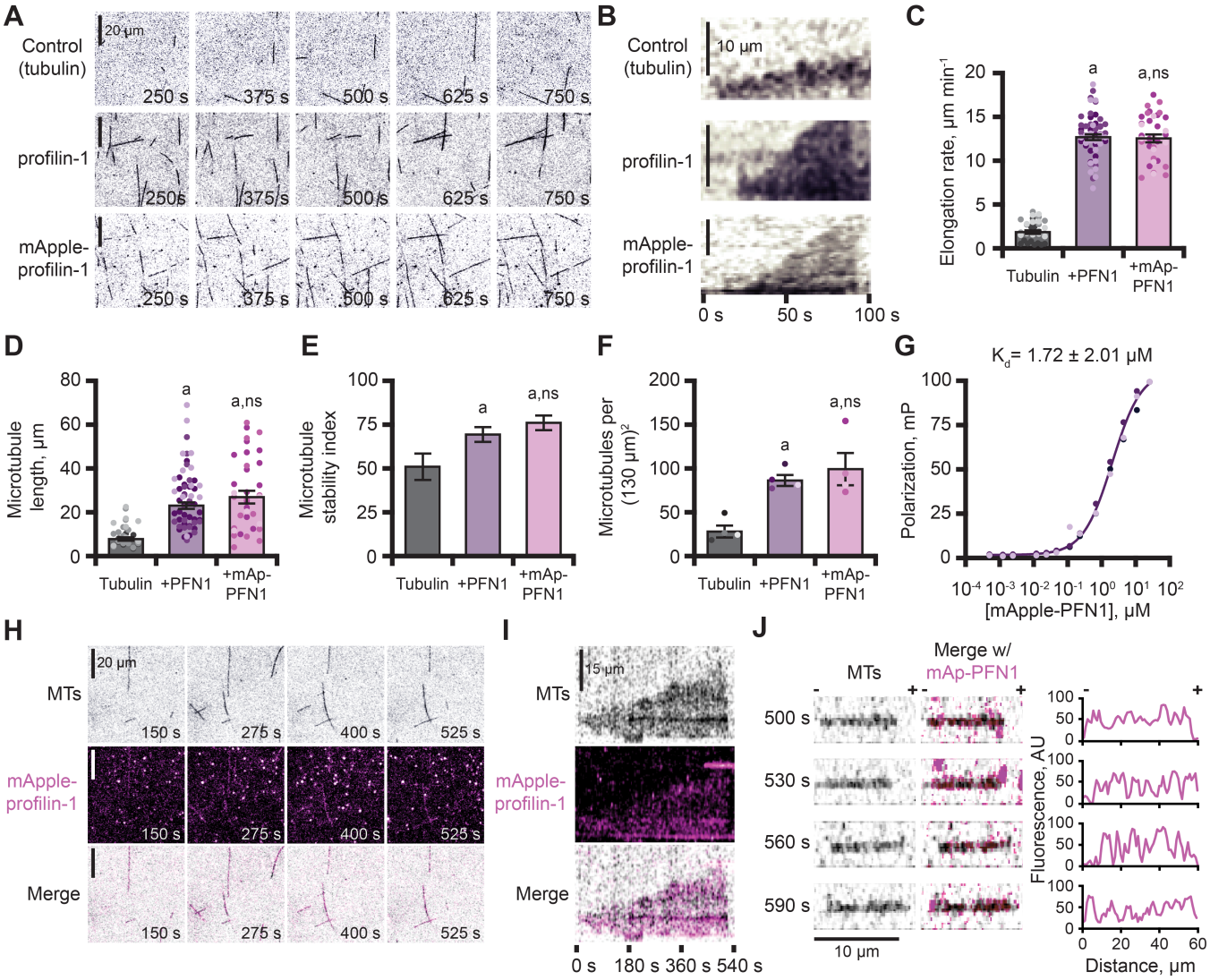

Fig. 5. Profilin binds tubulin dimers and associates with the microtubule lattice. (A) Representative views from TIRF reactions containing biotinylated GMP-CPP microtubule seeds, 10 µM free tubulin (5% Alexa-488-labeled) in the absence (control) or presence of 5 µM profilin or 5 µM mApple-profilin. Scale bars, 20 µm. See Supplemental Movie 5. **(B)** Kymographs from reactions as in (A) showing the growth of microtubules. Length scale bars, 10 µm. Elapsed time, 100 s. **(C)** Microtubule elongation rates measured in TIRF assays as in (A) (n = 35-58 microtubules). **(D)** Maximum length to which microtubules grew before undergoing catastrophe in TIRF assays as in (A) (n = 35-58 microtubules). **(E)** Microtubule stability index: rescue/catastrophe frequency (measured from n = 18-46 microtubules). **(F)** Total number of microtubules present in reactions as in (A) (n = 4 independent experiments). Shaded values represent the individual data points used to determine the mean from (n = 3) independent experiments. Error bars indicate SE. **(G)** Fluorescence anisotropy measurement of 10 nM unlabeled tubulin mixed with increasing concentrations of mApple-profilin. **(H)** Two-color views from TIRF reactions containing biotinylated GMP-CPP microtubule seeds, 10 µM free tubulin (5% Alexa-488-labeled) (black), and 5 µM mApple-profilin (pink). Scale bars, 20 µm. See Supplemental Movie 6. **(I)** Kymographs from two-color TIRF reactions as in (H) showing the growth of microtubules (MT). Scale bar, 15 µm. Elapsed time, 540 s. **(J)** Two-color montage of a single microtubule (black) and transiently bound mApple-profilin (pink) on the microtubule lattice. Fluorescence intensity profile from line scans along the microtubule from the mApple-profilin channel. + and - indicate the microtubule polarity. Scale bars, 10 µm. See Supplemental Movie 7. Significant differences by one-way ANOVA with Bartlett's correction for variance: ns, not significantly different from tubulin alone control; a, compared with control ($p < 0.05$); b, compared with untagged profilin (PFN1) ($p < 0.05$).

lin dimer addition to polymerizing microtubules.

We next tested whether specific regions, particularly the growing ends of microtubules, were enriched with mApple-profilin to facilitate polymerization. We performed two-color single-molecule TIRF microscopy and directly observed mApple-profilin and polymerizing microtubules (Figure 5H). A substantial amount mApple-profilin stuck to the imaging surface or was diffusely localized in the imaging plane. mApple-profilin was not enriched on the growing ends of microtubules. However, mApple-profilin bound and diffused along the microtubule lattice (Figures 5H-J). The observed profilin-microtubule side-binding interactions were extremely transient. Therefore, these results may not completely rule out profilin binding to the growing ends of microtubules to deposit dimers or stabilize tubulin dimers on growing protofilaments at timescales or at a resolution below our detection in these experiments. These results further support the idea that a fraction of available profilin is associated with the microtubule cytoskeleton. This suggests a mechanism where profilin may accelerate microtubule polymerization through direct interactions with tubulin dimers to promote microtubule assembly. Further profilin-microtubule interactions may stabilize growth through more transient lattice binding interactions.

Profilin regulates the morphology of N2a cells through actin and microtubule crosstalk.

To investigate whether our modified mApple-profilin could replace endogenous profilin-1 in cells, we generated two clonal CRISPR/Cas9 knockout cell lines for profilin-1 in Neuroblastoma-2a (N2a) cells (Figure 6). We used quantitative western blots to determine the bulk level of endogenous profilin as well as levels of profilin in CRISPR knockout cells following transfection with plasmids containing untagged profilin, mApple-profilin, or Halo-profilin (Figure 6A). While lipofectamine transfection has cell-to-cell variability, we frequently achieve 70-90 % transfection efficiency in these cells (Henty-Ridilla et al., 2016, 2017). Each CRISPR-generated profilin-deficient cell line proliferated significantly less efficiently than cells with endogenous profilin levels (Figure 6B), likely due to reported defects in the cell cycle (Suetsugu et al., 1998; Witke et al., 2001; Moens and Coumans, 2015). We performed quantitative western blot analysis to assess the efficiency of our rescue experiments. N2a cells contain 121 ± 15 μM profilin-1 (Figure 6C) and various rescue plasmids restored profilin protein to endogenous levels (Figures 6D-6E).

To confirm whether mApple-profilin could fully replace endogenous profilin in cells, we measured N2a cell morphology. We chose this parameter because N2a cells have unique actin filament and microtubule cytoskeletal features but do not efficiently perform other classic cell processes that require intact cytoskeletal crosstalk (i.e., migration or division). To standardize cell shape, we plated N2a cells on Y-shaped micropatterns and used spinning disk confocal super resolution microscopy (SoRa) and image deconvolution to visualize fixed cells. Profilin (PFN1$^{(-/-)}$) cells displayed aberrant morphologies significantly different from cells with endogenous or rescued profilin levels (Figure S6G). We created an overlay of binarized maximum intensity projections from each cell condition and quantified differences as the cell morphology index (the ratio of endogenous cell area to other cell conditions for cells plated on micropatterns of the same size) to emphasize that the condition of profilin does affect cellular structure or function (Figure S6H). Profilin-1$^{(-/-)}$ cells had significantly altered cell morphology compared to endogenous or mApple-profilin rescue cells ($p < 0.0001$) (Figure S6G and S6H). However, profilin-1$^{(-/-)}$ cells transfected with a plasmid harboring mApple-profilin exhibited morphologies not significantly different from untagged profilin ($p = 0.99$) (Figures S6G and S6H). We also assessed cells for broad differences in cytoskeletal architecture of actin filaments (Figures 6F and 6G) and microtubules (Figure 6H and 6I), using a similar morphology parameter. Unsurprisingly, the profilin-1$^{(-/-)}$ cells had strikingly aberrant actin filament ($p = 0.0008$) and microtubule networks ($p = 0.0006$) compared to cells with endogenous profilin levels (Figures 6H-6K). However, profilin-1$^{(-/-)}$ cells transfected with mApple-profilin displayed actin and microtubule morphologies that were not significantly altered from endogenous profilin-1$^{(+/+)}$ ($p = 0.98$) (Figures 6F-6I and S6G-H). Thus, our in vivo observations suggest that either tagged profilin (i.e., mApple or Halo-profilin) is functional for cytoskeleton-based activities in cells.

Profilin molecules associate with actin monomer-rich regions and microtubules in live cells.

Finally, to confirm the utility of these fluorescently-tagged profilins, we performed live-cell SoRa imaging on N2A cells expressing Halo-profilin-1. Profilin-1$^{(-/-)}$ cells were transfected with GFP-actin to simultaneously monitor monomeric and filamentous actin structures, EMTB-2×mChr to monitor microtubules, and Halo-profilin-1 using Janella Fluor-646 (JF-646) ligand to visualize profilin. At the recommended dilution of JF-646 ligand, profilin appeared localized throughout the cytoplasm and nucleus (Figure 7A). At best estimation, this concentration of JF-646 ligand only illuminates 2% of the total profilin present in a cell. However, no discrete localization to specific cytoskeletal or cell structures beyond the cytoplasm or nucleus can be discerned. To avoid the problem of high cytoplasmic profilin concentrations drowning out precise cellular localization signals and to test whether we could visualize specific pools of profilin, we titrated the JF-646 ligand in the imaging dish (Figure 7A). In most cells, at these nanomolar concentrations of JF-646 ligand, Halo-profilin appears localized to the cytoplasm, presumably associated with actin monomers (although this is well below the imaging resolution that we are currently able to achieve) (Figure 7A).

Intriguingly, in ~60% of the total cells imaged, Halo-profilin also appeared on filamentous structures coincident with the EMTB-2×mChr probe (microtubules) (Figures 7B and 7C).

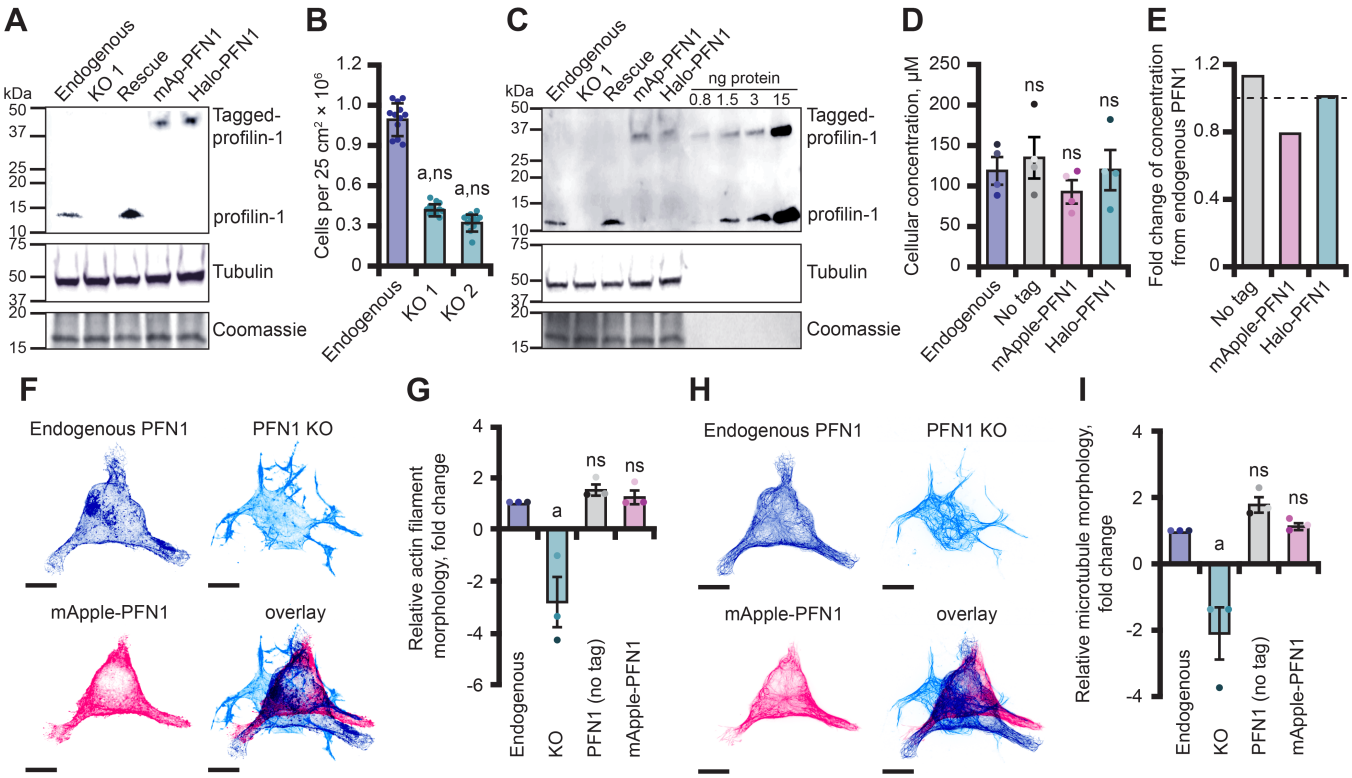

Fig. 6. Tagged profilin rescues cell morphology phenotypes present in profilin-deficient cells. (A) Western blot confirming CRISPR knockout and rescue of profilin-1 (PFN1) protein levels with either mAp-PFN1 or Halo-PFN1 constructs. N2a cell extracts were prepared from wild-type N2a (PFN1$^{(+/+)}$), profilin knockout (PFN1$^{(-/-)}$), or profilin knockout cells 24 h after transfection with a tag-less rescue construct, mAp-PFN1, or Halo-PFN1. Blots were probed with Profilin-1 B 10 primary (1:3,500 dilution; SantaCruz 137235) and goat anti-mouse 926-32210 secondary (1:5,000 dilution; LI-COR Biotechnology) antibodies. α-tubulin primary (1:10,000; Abcam 18251) and donkey anti-rabbit 926-68073 secondary (1:20,000) and the Coomassie stained membrane were used as a loading control. **(B)** Profilin-deficient cells proliferate less efficiently than cells with endogenous profilin levels. **(C)** Representative blot used to determine the concentration of endogenous profilin-1 in N2a cells. Blot was probed as in (A) compared to known quantities of purified mApple-profilin (43 kDa) or untagged profilin (15 kDa). Images of full blots are present in Figure S6. **(D)** Cellular concentration of endogenous profilin or several profilin rescue constructs (untagged, mApple-, or Halo-tags). Concentration was calculated from 100,000 cells and the volume of an N2a cell that we calculated as 196 (μm^3), similar to (Cadart et al., 2017). Mean values from four independent experiments ± SE shown. **(E)** Fold-change in profilin levels in PFN1$^{(-/-)}$ cells transfected with tagged or untagged profilin plasmids. Each construct rescues profilin protein levels to endogenous levels. **(F)** Super resolution confocal imaging of phalloidin-stained actin filaments from wild-type (endogenous; blue), profilin knockout (PFN1$^{(-/-)}$; cyan), or PFN1$^{(-/-)}$ transfected with mApple-PFN1 (pink) cells plated on Y micropatterns. N2a cells are shown individually and as an overlay aligned by the micropattern. Cells were imaged 24 h after transfection. At least 10 cells were analyzed per coverslip and n = 3 coverslips were analyzed per condition. **(G)** Quantification of actin morphology, calculated as a ratio of phalloidin-stained area from cells in (F) compared to endogenous control cells. PFN1$^{(-/-)}$ cells displayed significantly aberrant cytoskeletal morphology, cells rescued with mApple-profilin plasmid were not significantly different compared to endogenous controls (PFN1$^{(+/+)}$). **(H)** Tubulin immunofluorescence in the same N2a cells as in (F). α-tubulin was stained with 1:100 primary (Abcam 18251) and 1:100 fluorescently conjugated donkey anti-rabbit AlexaFluor-647 secondary (A31573; Life Technologies) antibodies. **(I)** Quantification of microtubule morphology of N2a cells plated similarly to (F). Error bars indicate SE across independent experiments (different coverslips). Significant differences by one-way ANOVA with Bartlett's correction for variance: ns, not significantly different from endogenous PFN1$^{(+/+)}$ control; a, compared with control ($p < 0.05$). Scale bars, 10 μm.

Expressing Halo-profilin over endogenous profilin to potentially saturate or shift the cellular profilin pools did not stimulate further microtubule association (Figure S7A and S7B). However, in this scenario not all profilin is able to be visualized. Therefore, this does not exclude the possibility that changes to profilin pools occurred, but were unable to be detected. To test the hypothesis that we could effectively shift profilin pools from the actin cytoskeleton to other cellular binding partners we transfected our profilin-1$^{(-/-)}$ knockout cells with several well characterized point-mutations known to disrupt specific facets of profilin-1 function, specifically: R88E, which does not bind actin monomers; G118V, which does not bind microtubules; and Y6D, which does not bind to poly-L-proline (PLP) tracks and thus, formin proteins (Ferron et al., 2007; Ezezika et al., 2009; Rotty et al., 2015; Henty-Ridilla et al., 2017). Removing the ability of profilin to bind actin monomers by expressing Halo-R88E led to a striking colocalization of profilin and microtubules in nearly all cells imaged (n > 50 cells from 5 separate experiments) (Figures 7B and 7C). While profilin and microtubules appear colocalized by line scans performed across the cell (Figure 7D), it is still difficult to determine whether these profilin molecules are moving along the microtubule lattice or associating and disassociating with individual microtubules. The localization of Halo-R88E to microtubules was so striking that we also expressed this mutant in cells with endogenous profilin-1$^{(+/+)}$, however the number of cells with profilin localized to microtubules was not significantly different (Figure S7A and S7B).

Profilin-1$^{(-/-)}$ knockout cells expressing Halo-G118V, had significantly less profilin associated with microtubules (Figure 7B and 7C). These cells displayed profilin aggregates, which are hypothesized to contribute to the onset of amyotrophic lateral sclerosis (ALS) in patients that have this amino acid substitution (Wu et al., 2012; Figley et al., 2014).

A line scan over a G118V expressing cell does not show localization coincident with microtubules except in instances where background ligand elsewhere is in the Z-axis of the acquired image. In contrast, >75% of profilin-1$^{(-/-)}$ cells expressing Halo-Y6D display localization of profilin on microtubules, and in the cytoplasm (Figures 7B and 7C). This is somewhat surprising because this construct of profilin should associate with actin monomers (Ferron et al., 2007). This observation may strengthen the hypothesis that the main cellular function for profilin is to stimulate actin assembly through formins or Ena/VASP (Rotty et al., 2015; Suarez et al., 2015; Funk et al., 2019; Skruber et al., 2020). Microtubules in these cells appear less dynamic than R88E-expressing cells, which may strengthen the hypothesis that profilin-microtubule interactions stabilize microtubule dynamics (Figure 7D).

Discussion

The lipid, actin, and microtubule regulating capabilities of profilin position it as a critical convergence point at the interface of major cell signaling pathways. However, the physiological significance for these findings has not been fully elucidated as previous methods used to tag profilin compromise different aspects of its function. Direct labeling approaches require several mutations and result in profilin aggregation (Vinson et al., 1998; Henty-Ridilla et al., 2017). Tagging directly on the C- or N-terminus disrupts PLP-binding (Wittenmayer et al., 2000). Splitting profilin to insert a fluorescence tag at a protruding loop in its tertiary structure results in a fusion protein that binds PLP and lipids with native affinity, but compromises actin binding (Nejedla et al., 2017). High cellular concentrations of profilin (121 μM for N2a cells measured here) further complicate physiological studies attempting to localize profilin in specific signaling schemes. As a consequence, the physiological roles of profilin have been largely understudied. Here we engineered a fluorescently-labeled profilin that binds PIP lipids, actin-monomers, and the PLP-motif containing formin protein. Labeled profilin suppresses spontaneous actin filament nucleation and stimulates formin-based actin polymerization at levels equivalent to untagged profilin. Using this tool, we unambiguously demonstrate that profilin is capable of directly binding to tubulin dimers and to the sides of growing microtubules, stimulating microtubule nucleation and elongation rates. Our genetic analyses in mammalian cells indicate that mApple-profilin and Halo-profilin are fully interchangeable with endogenous profilin and allow us to directly visualize individual molecules of dynamic profilin in live cells for the first time. Our data support a model where profilin mediates interactions between microtubule and actin systems at the level of individual cytoskeletal protein building blocks (i.e., actin monomers and tubulin dimers) (Figure 7E).

Here profilin was tagged with two different probes, mApple and a Halo-tag. These tags are entirely different, but we linked them to profilin using the same strategy and linker amino acid sequence. Therefore, it is likely that this strategy could be used in additional studies fusing profilin to other tags without losing functionality. This could be particularly exciting as new smaller (17 kDa) genetically encoded probes are developed or for using other probes that are closer in size to profilin (Oliinyk et al., 2019).

Profilin directly interacts with membranes through specific phosphoinositide lipids to modulate cellular actin and microtubule dynamics (Sun et al., 2013; Pinto-Costa and Sousa, 2019; Davey and Moens, 2020). PI(4,5)P_2, is the predominant signaling lipid present in cells and it recruits profilin (and profilin ligands including formin and tubulin) directly to the plasma membrane (Popov et al., 2002; Janmey et al., 2018; Davey and Moens, 2020). Binding of actin or proline-rich ligands release profilin from PI(4,5)P_2 present in plasma membrane to regulate cell signaling pathways (Lambrechts et al., 2002; Krishnan and Moens, 2009). PI(3,5)P_2 is a low abundance PIP localized on late endosomes and lysosomes (Davey and Moens, 2020) and is considered a critical convergence point between intracellular membrane dynamics, signal transduction, and the cytoskeleton (Ikonomov et al., 2006; Michell et al., 2006). Our tagged versions of profilin maintain full binding capacity for PI(4,5)P_2 and PI(3,5)P_2 lipids (Figure 2E), which is a critical facet of cellular signal transduction cascades involving profilin in several human diseases including Charcot-Marie-Tooth, amyotrophic lateral sclerosis (ALS), and cancers (Bolino et al., 2000; Pimm et al., 2020).

Using mApple-profilin in biochemical assays, we learned that profilin binds sides of microtubules and also directly to tubulin dimers (Figure 7E). With this evidence in mind, an attractive model to explain how profilin enhances microtubule polymerization is that the higher affinity of mApple-profilin for tubulin dimers (k_D = 1.7 μM) and more efficiently organizes dimer addition to microtubules. This may accelerate microtubule assembly from protofilaments or at microtubule plus-ends. Once assembled, profilin may remain associated with the microtubule lattice to stabilize lateral contacts along the lattice. This may also confirm the hypothesis that profilin lowers the critical concentration required for microtubule assembly (Henty-Ridilla et al., 2017; Nejedlá et al., 2021).

Profilin is a classical inhibitor of spontaneous actin formation, thus blocking actin assembly through steric interactions (Cooper et al., 1984; Ferron et al., 2007). Additionally, in vitro studies revealed a fierce competition among actin filament nucleation systems (i.e., formins, Ena/VASP, or the Arp2/3 Complex) for profilin-bound actin monomers to ultimately dictate whether linear or branched actin networks are formed (Rotty et al., 2015; Suarez et al., 2015). Genetic studies in yeast further corroborated these competitive internetwork dynamics (Suarez and Kovar, 2016). However, yeast lack thymosin-β4, a high affinity ligand that outcompetes profilin for actin monomers (20-fold higher affinity) (Figure 3A; Jean et al., 1994; Skruber et al., 2018; Pimm et al., 2020). Elegant work precisely tuning the concentrations of profilin in mammalian cells resulted in polymerization of discrete actin networks at the leading edge (Skruber et al., 2020). Given the presence of PI(4,5)P_2 at the plasma mem-

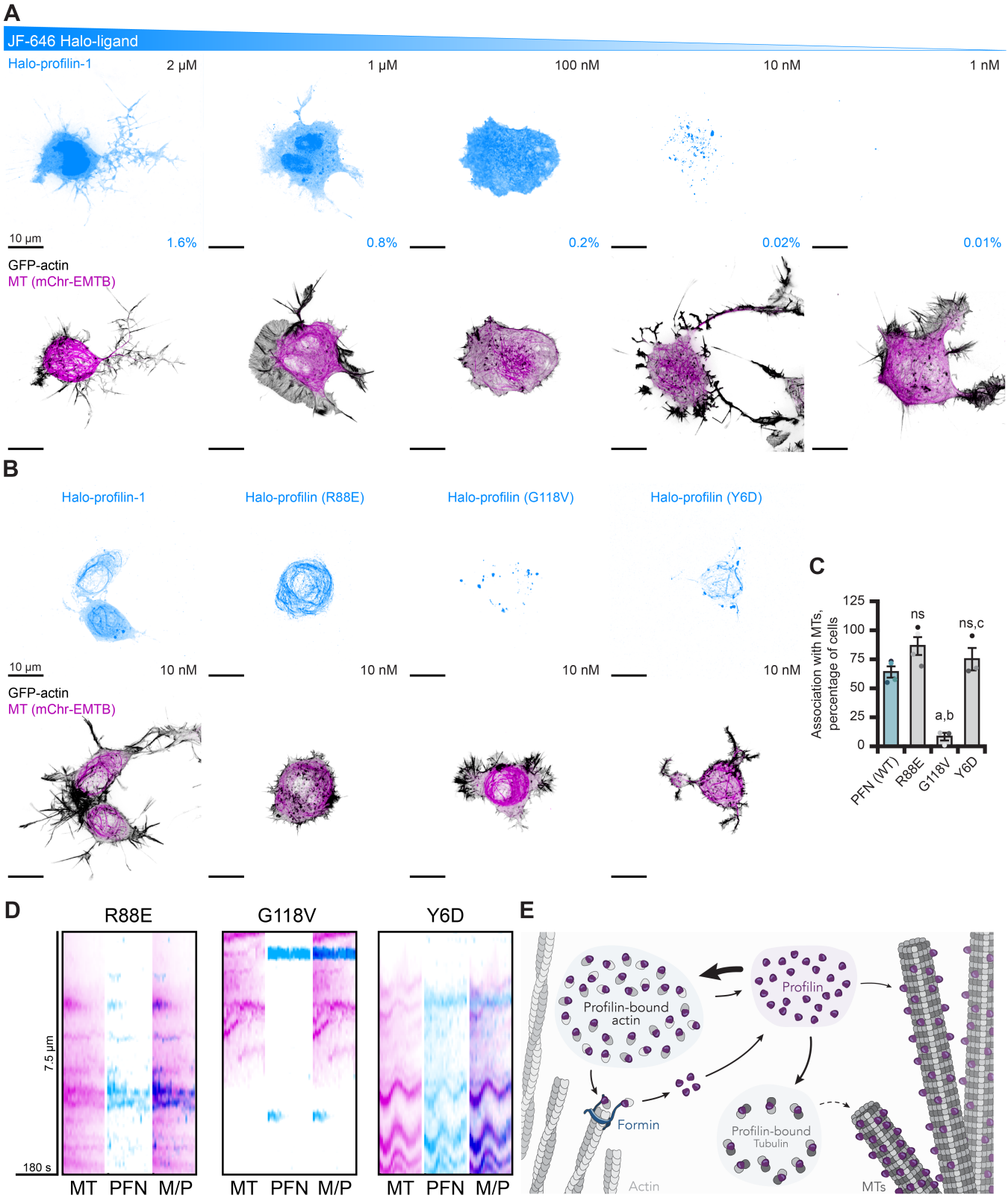

Fig. 7. Live-cell visualization of individual molecules of profilin. (A) Maximum intensity Z-projections of SoRa spinning disk confocal imaged profilin-1$^{(-/-)}$ knockout cells (N2a) transiently expressing GFP-actin (black), ensconsin microtubule binding domain (EMTB)-2×mCherry (microtubules; magenta), and JF-646 labeled Halo-profilin-1 (light blue). The final concentration of Halo-ligand in each imaging dish (black, upper right corner) and conservative over estimation of the total amount of profilin visualized with concentrations of Halo-ligand (light blue, lower right corner) is shown. 10 nM Halo-ligand was used to visualize a subset of total cellular profilin for all subsequent analyzes. **(B)** Halo-profilin-1 constructs (WT, R88E, G118V, and Y6D; visualized with 10 nM JF-646 ligand) transiently expressed in N2a cells imaged and presented identically to cells in (A). Scale bars, 10 µm. **(C)** The bottom 2 µm of Z-projections from cells in (B) were scored for association (pixel overlap) with microtubules (faint or bright). **(D)** Kymographs displaying overall cellular dynamics for a single 7.5 µm line scan through cells (line placement shown in Figure S7C). Time represented is 180 s. **(E)** Model for profilin distribution between actin and microtubules. Actin monomers, actin filament nucleators (i.e., formin or Ena/VASP), microtubules, and tubulin dimers all compete for free profilin in a cell. This competition dictates higher-order actin-microtubule crosstalk in cells.

brane, the preferred mechanism of actin assembly in cells is profilin dependent, using formin proteins (Suarez et al., 2015; Funk et al., 2019; Skruber et al., 2020). Indeed, our functional Halo-profilin permits direct visualization of this dynamic competition and collaboration between actin filament nucleation systems (Figure 7B-D). Specifically, using Halo-profilin-1(R88E) shifts profilin from the actin cytoskeleton to microtubules and Halo-profilin-1(Y6D) shifts profilin toward microtubules by disrupting interactions between profilin and formin and/or Ena/VASP (Figure 7B-D).

Initial observations of profilin-microtubule association in cells were thought to be indirect, based largely on localization experiments performed using the pan-formin inhibitor, SMIFH2 (Nejedla et al., 2016; Nejedlá et al., 2021). As a result, the cellular association between profilin and microtubules would likely be mediated by one or more of the fifteen mammalian formin proteins. Evidence now suggests SMIFH2 treatments disrupt additional cytoskeletal regulation proteins (i.e., myosins and p53) besides formin proteins (Isogai et al., 2015; Nishimura et al., 2021). Here, we were able to visualize Halo-profilin on the sides of microtubules in most N2a cells (Figure 7). We used a genetic approach, expressing well-characterized point mutants in profilin that disrupt specific facets of profilin function. With Halo-profilin-1(R88E) that does not bind actin monomers, we observed an increase in profilin-microtubule localization (Figures 3B, 3C, and 4G). This finding agrees with binding affinities of profilin for either actin or microtubules determined from in vitro experiments. In addition, the Halo-profilin-1(Y6D) construct may further strengthen the idea that profilin-microtubule association is executed through direct binding or through means other than formin proteins (Figure 7B-D).

Many cell processes that rely on the functional interplay between actin and microtubules are also mediated through profilin (Pinto-Costa and Sousa, 2019; Davey and Moens, 2020; Pimm et al., 2020; Karlsson and Dráber, 2021; Pimm and Henty-Ridilla, 2021). Profilin colocalizes to the sides of microtubules in several cell types (Di Nardo et al., 2000; Grenklo et al., 2004; Nejedla et al., 2016). Profilin is also present at centrosomes in B16 cells bound to the microtubule nucleation complex γ-TuRC (Consolati et al., 2020; Karlsson and Dráber, 2021; Nejedlá et al., 2021). Depending on the cell type, overexpression of profilin stimulates the mean growth rate of cellular microtubules up to 5-fold (Nejedla et al., 2016; Henty-Ridilla et al., 2017). While the Halo-profilin-1(R88E) promoted strong profilin-microtubule association, a large proportion of cells expressing Halo-profilin-1 also displayed microtubule localization. Thus, the actin-binding deficient point-mutation is not required for localization. Several disease-variants of profilin have been identified in cancer and neurodegenerative disorders (Michaelsen-Preusse et al., 2016; Pimm et al., 2020). This tagging strategy allowed us to visualize the first substantial cytoskeleton-based phenotype for the ALS-associated profilin-1 variant, G118V – a loss in association between profilin and microtubules. Thus, we anticipate these tools (i.e., mApple-, Halo-, or Halo(mutant)-profilin-1) will be useful for the future exploration of profilin-based mechanisms in important cell processes, disease-states, or in vitro analyses.

Methods

Reagents.

All materials were obtained from Fisher Scientific (Waltham, MA) unless otherwise noted.

Plasmid construction.

Purified DNA from a vector containing full-length mApple (mApple-C1 vector; Kremers et al., 2009) was PCR amplified with the following primers to generate overlapping ends: forward: 5'- CTTTAAGAAGGAGATAT ACATATGGTGAGCAAGGGCGAGG-3'; and, reverse: 5'- CCACCCGGCCATGGAAGCTTGAGC -3'. DNA fragments of full-length mApple containing overlapping ends and NdeI-linearized pMW172 containing the full-length sequence of human profilin-1 (NCBI Gene ID: 5216; Eads et al., 1998; Henty-Ridilla et al., 2017) were joined via Gibson assembly according to manufacturer's instructions (NEB, Ipswich, MA). The final cassette is an N-terminal mApple fluorescent protein, followed by a ten amino acid spacer, and profilin-1, that is flanked by NdeI and EcoRI restriction sites. Mammalian expression vectors were generated by Genscript (Piscataway, NJ) as follows: the mApple-profilin cassette was synthesized and inserted into the backbone of mApple-C1 behind the CMV promoter at the Ndel and BamHI restriction sites, replacing the original mApple sequence; For Halo-profilin, the ten amino acid linker and profilin-1 was synthesized and inserted into the backbone of a pcDNA-Halo expression vector (provided by Gunther Hollopeter, Cornell University) at the KpnI and NotI restriction sites. The Y6D, R88E, G118V point mutants in Halo-profilin-1 were generated by site-directed mutagenesis (Genscript). The final sequence for each plasmid constructed above was verified by Sanger sequencing (Genewiz, South Plainfield, NJ).

Protein purification.

Profilin constructs (untagged or mApple-profilin) were transformed and expressed in Rosetta2(DE3) (Millipore-Sigma, Burlington, MA) competent cells. Cells were grown in Terrific Broth to OD600 = 0.6 at 37 °C, then induced with IPTG for 18 h at 18 °C. Cells were collected by centrifugation and stored at -80 °C until purification. Cell pellets were resuspended in 50 mM Tris HCl (pH 8.0), 10 mg/mL DNase I, 20 mg/mL PMSF, and 1× protease inhibitor cocktail (0.5 mg/mL Leupeptin, 1000 U/mL Aprotinin, 0.5 mg/mL Pepstatin A, 0.5 mg/mL Antipain, 0.5 mg/mL Chymostatin). Cells were incubated with 1 mg/mL lysozyme for 30 min and then lysed on ice with a probe sonicator at 100 mW for 90 s. The cell lysate was clarified by centrifugation at 278,000 × g. The supernatant was passed over a QHighTrap column (Cytiva, Marlborough, MA) equilibrated in 50 mM

Tris-HCl (pH 8.0), 1 M KCl. Profilin was collected in the flow through and then applied to a Superdex 75 (10/300) gel filtration column (Cytiva) equilibrated in 50 mM Tris (pH 8.0), 50 mM KCl. Fractions containing profilin were pooled, aliquoted, and stored at 80 °C.

N-terminally tagged 6×His-GFP-thymosin-β4 (GFP-Tβ4) was synthesized and cloned into a modified pET23b vector at the AgeI and NotI restriction sites (Genscript). Bacteria were transformed, induced, collected, and stored as described for profilin (above). Cell pellets were resuspended in lysis buffer (2× PBS (pH 8.0) (2.8 M NaCl, 50 mM KCl, 200 mM sodium dibasic, 35 mM potassium monobasic), 20 mM Imidazole (pH 7.4), 500 mM NaCl, 0.1% Triton-X 100, 14 mM BME) and lysed as above. Lysate was clarified via centrifugation for 30 min at 20,000 x g and the supernatant was flowed over Cobalt affinity columns (Cytiva) equilibrated in low imidazole buffer (1× PBS (pH 8.0) supplemented with 20 mM Imidazole (pH 7.4), 500 mM NaCl, 0.1% Triton-X 100, 14 mM BME). GFP-Tβ4 was eluted using a linear gradient into high imidazole buffer (1× PBS (pH 8.0) supplemented with 300 mM Imidazole (pH 7.4), 150 mM NaCl, 0.1% Triton-X 100, 14 mM BME) and the 6×His-tag was cleaved with 5 mg/mL ULP1 protease for 2 h at 4 °C, concentrated, and applied to a Superdex 75 (10/300) gel filtration column equilibrated with GF buffer (1× PBS (pH 8.0) supplemented with 150 mM NaCl, 14 mM BME). Fractions containing GFP-Tβ4 were pooled, aliquoted and stored at -80 °C.

The constitutively active formin 6×His-mDia1(FH1-C) (amino acids 571-1255) was synthesized and cloned into modified pET23b vector at the AgeI and NotI restriction sites (Genscript). Bacteria were transformed, induced, and collected as described for profilin and GFP-Tβ4. The protein was purified as described for GFP-Tβ4, with the exception of applying the cleaved formin to a Superose 6 Increase (10/300) gel filtration column (Cytiva). Fractions containing mDia1(FH1-C) were pooled, aliquoted, and stored at -80 °C.

Rabbit skeletal muscle actin (RMA), Oregon-Green (OG) labeled-actin, and N-(1-pyrenyl)iodoacetamide (pyrene) actin were purified from acetone powder as described in detail (Spudich and Watt, 1971; Cooper et al., 1984; Henty-Ridilla et al., 2017), however rather than starting with frozen tissue, fresh rabbit muscle (Side Hill Farmers, Manlius, NY) was used. Alexa-647-actin was labeled on lysine residues as follows: 5 g of acetone powder was rehydrated in G-buffer (3 mM Tris pH 8.0, 0.5 mM DTT, 0.2 M ATP, 0.1 mM $CaCl_2$) for 60 min on ice. Actin was polymerized from the supernatant overnight at 4 °C with the addition of 2 mM $MgCl_2$, 50 mM NaCl and 0.5 mM ATP. The following day, the concentration of NaCl was adjusted to 0.6 M, the polymerized actin was collected by centrifugation at 361,000 × g, and then depolymerized by dounce homogenization and dialysis against G-buffer for 24 h at 4 °C. Dialysis buffer was replaced with labeling buffer (100 mM PIPES-Tris (pH 6.8), 100 mM KCl, 0.4 mM ATP, 0.4 mM $CaCl_2$) for 2 h at 4 °C and exchanged twice. Dialyzed actin was polymerized by adding 1 mM $MgCl_2$ and 50 mM KCl and labeled with a 5-20-fold excess of NHS-Alexa-647 for 18 h at 4 °C. Labeled actin filaments were depolymerized by dounce homogenization and dialysis as above, precleared at 435,000 × g, and loaded onto a HiPrep S200 (16/60) gel filtration column (Cytiva) equilibrated in G-Buffer. Fractions containing labeled actin were pooled and dialyzed against G-buffer supplemented with 50% glycerol and stored at 4 °C. All purified actins were pre-cleared at 279,000 × g before use.

Tubulin was purified from freshly obtained Bovine brains by three cycles of temperature-induced polymerization and depolymerization as described in detail (Castoldi and Popov, 2003). Fluorescently labeled tubulin was purchased from Cytoskeleton, Inc (Denver, CO), and resuspended according to manufacturer's instructions. AlexaFluor-647 GMP-CPP microtubule seeds were polymerized by combining 15 μM unlabeled tubulin, 7.5 μM AlexaFluor-647 tubulin, 7.5 μM biotin-tubulin, and 0.5 mM GpCpp (Jena Bioscience, Jena, Germany) and incubating for 30 min at 37 °C (Groen et al., 2014). Seeds were collected by centrifugation and resuspended in 1×BRB80 (80 mM PIPES, 1 mM MgCl2, 1 mM EGTA, pH 6.8 with KOH), aliquoted, and stored at 80 °C. Unlabeled tubulin was recycled before use in TIRF microscopy assays (Castoldi and Popov, 2003).

All protein concentrations were determined by band densitometry from Coomassie-stained SDS-PAGE gels, compared to a BSA standard curve. Band intensities were quantified using a LI-COR Odyssey imaging system (LI-COR Biotechnology, Lincoln, NE). Labeling stoichiometries were determined using the spectroscopy, molar extinction coefficients, and predetermined correction factors, as follows: unlabeled actin ε_{290} = 25,974 M^{-1} cm^{-1}, Oregon Green ε_{496} = 70,000 M^{-1} cm^{-1}, Alexa-650 = 239,000 M^{-1} cm^{-1}. The correction factor used for Oregon Green was 0.12, and for Alexa-647 was 0.03.

Liposome preparation and pelleting assays.

Liposomes (Avanti Polar lipids, Alabaster, AL) of defined PIP lipid content were prepared according to (Banerjee and Kane, 2017). Briefly, powdered lipids were resuspended in CH_3OH:$CHCl_3$:H_2O at a 9:20:1 ratio. Liposomes contained 55% (mol %) 16:0 phosphatidylcholine, 25% 16:0 phosphatidylserine (PS), 18% 16:0 phosphatidylethnolamine, and 5% 18:1 (0.33 mM final concentration) phosphatidylinositol phosphates (PI(3,5)P_2 or PI(4,5)P_2). Control liposomes did not contain PIPs but did contain 16:0 phosphatidylserine. The mixed lipids were dried using a centrivap lyophilizer with a vacuum pump at 35 °C for 30–40 min. Lyophilized lipids were resuspended and in ice-cold liposome buffer (25 mM NaCl, pH 7.4, 50 mM Tris-HCl), and then subjected to five freeze-thaw cycles. Finally, liposomes were extruded through a 100 nm filter 20 times. 1 μM profilin (untagged or mApple-profilin) was mixed with 0.33 mM PIP liposomes in resuspension buffer (50 mM Tris, pH 8.0; 150 mM KCl; 10 mM DTT). The solution was incubated at room temperature for 30 min, then liposomes were pelleted via centrifugation at 400,000 × g for 30 min. The supernatant

and pellet fractions were separated and then the pellet was resuspended in an equal volume (i.e., 100 µL) of buffer. Samples were precipitated using 10%(v/v) trichloroacetic acid, washed with cold acetone, and dissolved in 50 µL of cracking buffer (50 mM Tris-HCl, pH 6.8, 8 M urea, 5% SDS, and 1 mM EDTA). Each sample was separated by SDS-PAGE electrophoresis and transferred into nitrocellulose membrane. The resulting blots were probed with 1:5,000 profilin-1 anti-mouse 137235 primary (SantaCruz Biotechnology, Dallas, TX) and 1:10,000 IRDye 800 Goat anti-mouse 926-32210 secondary (LI-COR Biotechnology, Lincoln, NE) antibodies. Antibodies recognizing profilin were detected using a LI-COR Odyssey Fc imaging system and quantified by densitometry in Fiji (Schindelin et al., 2012).

Fluorescence anisotropy binding assays.

Direct actin-binding experiments were performed in binding mix (1× PBS (pH 8.0) supplemented with 150 mM NaCl). Reactions with actin (10 nM) (unlabeled or OG-labeled) were incubated at room temperature for 15 min and anisotropy was determined by exciting at 440 nm and measuring emission intensity at 510 nm with bandwidths set to 20 nm using a Tecan plate reader (Tecan, Männedorf, Switzerland) equipped with a monochromator. Competitive actin-binding experiments contained 10 nM unlabeled actin and 10 nM GFP-Tβ4 with variable concentrations of unlabeled profilin or mApple-profilin. Direct binding analyses utilizing mApple-profilin (various concentrations) were measured using 568 nm excitation and 592 nm emission with bandwidths set to 20 nm. Direct tubulin-binding experiments were performed with 10 nM tubulin in 1×BRB80 supplemented with 150 mM NaCl. Reactions were incubated at 4 °C for 30 min before reading. Reactions containing tubulin were screened for the presence of microtubules at the conclusion of the experiment. No microtubules were present in any condition. Reactions with all proteins were precleared via centrifugation at 279,000 × g before use.

Bulk actin assembly assays.

Bulk actin assembly assays were performed by combining freshly recycled 2 µM monomeric Mg-ATP actin (5% pyrene labeled), proteins or control buffers, and initiation mix (2 mM $MgCl_2$, 0.5 mM ATP, 50 mM KCl). Reactions for each replicate were initiated simultaneously by adding actin to reactions using a multichannel pipette. Total fluorescence was monitored using excitation 365 nm and emission 407 nm in a Tecan plate reader. Recorded values were averaged between three replicates. Shaded areas represent the standard deviation between replicates.

In vitro TIRF microscopy assays.

TIRF microscopy flow cells were prepared by attaching PEG-silane coated coverslips to µ-Slide VI0.1 (0.1 mm × 17 mm × 1 mm) flow chambers (Ibidi, Martinsried, Germany) with 120 µm thick double-sided tape (2.5 cm × 2 mm × 120 µm) (Grace Bio-Labs, Bend, OR) and 5-minute epoxy (Devcon, Riviera Beach, FL) (Smith et al., 2013). Imaging chambers were conditioned as follows: 1% BSA, 4 µg/mL streptavidin in 10 mM Tris-HCl (pH 8.0), 1% BSA, and then 1× TIRF buffer supplemented with 0.25% methylcellulose [4000 cP] for actin (20 mM imidazole (pH 7.4) 50 mM KCl, 1 mM MgCl2, 1 mM EGTA, 0.2 mM ATP, 10 mM DTT, 40 mM glucose) or microtubules (1× BRB80, 50 mM KCl, 0.1 mM GTP, 10 mM DTT, 40 mM glucose). Time lapse TIRF microscopy was performed using a DMi8 inverted microscope equipped with 120-150 mW solid-state lasers, a 100× Plan Apo 1.47 N.A. oil-immersion TIRF objective (Leica Microsystems, Wetzlar, Germany), and an iXon Life 897 EMCCD camera (Andor; Belfast, Northern Ireland). Focus was maintained using the adaptive focus system (Leica Microsystems, Wetzlar, Germany), and frames were captured at 5 s intervals. Reactions visualizing actin used 50 ms exposure, 488 nm or 647 nm excitations. For microtubules settings were 100 ms exposure, 488 nM excitation, 10% laser power. Reactions visualizing mApple-profilin used 100 ms exposure, 561 nM excitation, with 5% laser power. Reactions were introduced into the flow chamber using a luer lock system on the coverslip directly mounted on the microscope stage, and flow was achieved with a syringe pump (Harvard Apparatus, Holliston, MA). All reactions are timed from the initial mixing of proteins rather than the start of image acquisition (usually delayed by 15-20 s). Reactions containing actin were performed at room temperature. Reactions with growing microtubules were performed at 35 °C, maintained by a stage and objective heater system (OKO lab, Pozzuoli, Italy). Actin and microtubules were loosely tethered to the cover glass surface using an avidin-biotin conjugation system. Dynamic parameters for actin or microtubules were determined by analyzing TIRF movies in Fiji (Schindelin et al., 2012). Actin nucleation was measured as the number of actin filaments present 100 s after the initiation of the reaction. Actin filament elongation rates were measured as the slope of a line generated from the length (µm) of actin filaments over time for at least four consecutive movie frames. This number was multiplied by the number of actin subunits per micron, previously calculated as 370 subunits (Pollard et al., 2000). Microtubule length measurements and elongation rates (microns per min) were determined from kymographs as the change in microtubule length divided by time spent growing. Microtubule stability index was calculated as the ratio of catastrophe events divided by the number of rescue events.

Mammalian cell culture, confocal microscopy, and imaging analysis.

Neuroblastoma (N2a) cells were grown in DMEM supplemented with 200 mM L-glutamine, and 10% FBS. Transfections were performed using Lipofectamine 3000 according to manufacturer's instructions for 6-well plates using 75,000 cells and 100-200 ng plasmid per well. Cells

were lysed (for western blots) or imaged 18-24 h following transfection. Pooled profilin-1 CRISPR and comparable wild-type N2a cells (Synthego, Menlo Park, CA) were diluted to an average of 0.5 cells per well and further screened via western blot for clonal profilin-1 knockout lines using identical conditions as described for quantitative western blots, below. For cell counts, wild-type and profilin-1$^{(-/-)}$ knockout cells were seeded at 100,000 cells per T25 flask (Genesee Scientific, San Diego, CA), passaged, and counted every 4 d.

100,000 cells were plated on medium-sized fibronectin coated Y-patterned coverslips (CYTOO, Inc., Grenoble, France). After 4 h unbound cells were aspirated, and remaining attached cells were fixed in 8% glutaraldehyde diluted in 1x PBS. Autofluorescence was quenched with freshly prepared 0.1%(w/v) sodium borohydride. Microtubules were visualized by immunofluorescence as follows. Fixed cells were permeabilized in 1× PBS supplemented with 0.25% Triton X-100, blocked for 1 h in 1% BSA (w/v) diluted in PBST (1× PBS supplemented with 0.1% Tween (v/v)) and incubated with 1:250 anti-rabbit primary antibody 18251 against α-tubulin (Abcam, Cambridge, UK) for 16 h. Coverslips were washed with 1× PBST and incubated for 1 h with a combination of: 1:500 donkey anti-rabbit secondary antibody AlexaFluor-568 and 1:500 AlexaFluor-647 phalloidin to stain actin filaments. Coverslips were mounted in AquaMount.

Fixed cells were imaged by spinning disk confocal super resolution (SoRa) microscopy on an inverted Nikon Ti2-E microscope (Nikon Instruments, Melville, NY) equipped with a compact 4-line laser source (405 nm, 488 nm, 561 nm, and 640 nm wavelengths), a CF160 Plan Apo 60× 1.4 N.A. oil-immersion objective, a CSU-W1 imaging head (Yokogawa Instruments, Tokyo, Japan), a SoRa disk (Nikon Instruments, Melville, NY), and a Prime BSI sCMOS camera with a pixel size of 6.5 µm/pixel (Teledyne Photometrics, Tucson, AZ). Images were acquired using Nikon Elements software with artificial intelligence analysis modules. Maximum intensity projections and fluorescence subtraction for cell, actin, and microtubule morphologies was performed using Fiji (Schindelin et al., 2012). Briefly, cell images were acquired and the threshold was set to identical levels for each set of comparisons (i.e., the same settings were used for microtubule comparisons but these settings were not identical to those used for actin comparisons). Masks of cells with endogenous profilin were aligned by the micropattern shape and overlaid on profilin knockout or profilin-1 knockout cells expressing tagged and untagged profilin expression plasmids. Thus, the morphology index is the ratio of total pixels in the actin or microtubule channel of control cells with endogenous profilin, compared cells lacking profilin-1, or knockout cells expressing mApple-profilin-1 or Halo-profilin-1 DNA plasmids. Mean ratios from three different coverslips (and at least 10 cells per coverslip) are shown.

Live-cell experiments were imaged by SoRa microscopy as above. N2A cells were plated in glass-bottom 35 mm dishes (MatTek, Ashland, MA). Transfections were performed using Lipofectamine 3000 according to manufacturer's instructions for 6-well plates using 42,000 cells and 100 ng of the following plasmids per well: reduced expression GFP-beta-actin (Watanabe and Mitchison, 2002), ensconsin-microtubule binding domain (EMTB)-2×mCherry (Miller and Bement, 2009), and constructs of Halo-profilin. Thirty minutes prior to imaging DMEM growth media was replaced with HEPES (pH 7.4)-buffered DMEM lacking phenol red. Cell temperature was maintained at 37 °C for the duration of the experiment with a stage heater insert (OKO labs, Ambridge, PA). Janella Fluor 646 (Promega) was resuspended according to manufacturer's directions. Stock Halo-ligands were diluted directly into imaging dishes and incubated for 5 minutes before image acquisition. We found Halo-ligand titrations varied depending on what Halo-ligand was being used. Thus, all observations in Figure 7 use the same batch of JF-646. Dilutions for the titration experiments were performed in DMEM media before being directly added to each imaging dish. Dishes were imaged a maximum of 60 min. Live-cell 4D movies were generated from Z-stacks of the bottom 2 µm of cells (adjacent to the cover glass) with Richardson-Lucy deconvolution (40-interactions for each movie, identical image acquisition).

Determination of cellular profilin concentrations.

The concentration of profilin, mApple-profilin, or Halo-profilin in N2a cells was determined using quantitative western blots. 100,000 cells were seeded and then grown to confluency in 6-well plates and lysed in equal volumes of 2× Laemmli buffer. Equal volumes of cell lysate per condition were loaded on SDS-PAGE gels alongside a profilin standard curve. Lysates were not corrected for transformation efficiency; however, transformation efficiencies were typically between 70-90% of the total cells plated. Blots were probed with a 1:3500 dilution of profilin-1 anti-mouse 137235 primary antibody (Santa Cruz Biotechnology, Inc.) for 16 h. Blots were washed three times and probed with 1:6000 IRDye 800 Goat anti-mouse 926-32210 secondary antibody (LI-COR Biotechnology) for 1 h at room temperature and washed again. Fluorescent secondary antibodies recognizing profilin were detected using a LI-COR Odyssey Fc imaging system and quantified by densitometry in Fiji (Schindelin et al., 2012). The amount of profilin was determined by comparing levels to the standard curve. Values were averaged from four independent blots. The mean cell volume of a typical N2a cell was calculated as 196 µm3 (1.96 × 10-13 L) by taking the average XY area of ten well-spread N2a cells and then multiplying by the mean cell thickness in Z (~1 µm) from the same cells, similar to (Christ et al., 2010; Cadart et al., 2017).

Data analyses and availability.

GraphPad Prism 9 (GraphPad Software, San Diego, CA) was used for all data analyses and to perform all statistical tests. Non-linear curve fits for anisotropy experiments

were performed using data normalized so that the smallest mean in each data set was defined as zero. Data were fit to the following curve using least squares regression with no constraints: $Y = Y_0 - B_{max}*(X/(K_D+X))$. The specific details for each experimental design, sample size, and specific statistical tests are available in the figure legends. All datasets were tested for normality before performing t-tests or ANOVA. P-values lower than 0.05 were considered significant for all analyses. Individual data points are included for each figure. Different shades of colored data points show technical replicates from separate experimental runs. Darkest shading in different conditions represents experiments that can be compared from the same experimental dataset. Datasets for each figure have been deposited in the Zenodo Henty-Ridilla laboratory community, available here: http://doi.org/10.5281/zenodo.5329585. Access will be granted upon reasonable request.

Supplemental information

Supplemental information includes 7 figures and 8 movies.

Author contributions

M.L.P, X.L., F.T., and J.L.H-R performed the experiments. M.L.P, X.L., A.L., F.T., and J.L.H-R analyzed the experiments. J.L.H-R designed experiments, supervised, and obtained funding for this work. J.L.H-R wrote the manuscript.

Competing interests

The authors declare no competing interests.

Acknowledgements

We are grateful to Marc Ridilla (Repair Biotechnologies) and Brian Haarer (SUNY Upstate) for comments on this manuscript. We are also grateful for ASAPbio, specifically: Iratxe Puebla (ASAPbio), Ricardo Carvalho (Simon Fraser University), Joachim Goedhart (University of Amsterdam), Sónia Gomes Pereira (University of Geneva), Pratima Gurung (Harvard Medical School), Samuel Lord (University of California, San Francisco), Claudia Molina (Icahn School of Medicine at Mount Sinai), Arthur Molines (University of California, San Francisco), Gregory Redpath (University of Otago), Mugdha Sathe (University of Washington), Sagar Varankar (University of Cambridge), and Ewa Sitarska (European Molecular Biology Laboratory), for providing a crowd sourced peer review. This research was funded by a Sinsheimer Scholar Award, Amyotrophic Lateral Sclerosis Association Starter Grant (20-IIP-506), and NIHR35 GM133485.

References

1. Aguda, AH, Xue, B, Irobi, E, Préat, T, and Robinson, RC (2006). The structural basis of actin interaction with multiple WH2/β-thymosin motif-containing proteins. Structure 14, 469–476.
2. Antoine, M et al. (2020). Splicing defects of the profilin gene alter actin dynamics in an S. pombe SMN Mutant. iScience 23, 100809.
3. Banerjee, S, and Kane, PM (2017). Direct interaction of the Golgi V-ATPase a-subunit isoform with PI(4)P drives localization of Golgi V-ATPases in yeast. Mol Biol Cell 28, 2518–2530.
4. Bindels, DS et al. (2017). mScarlet: a bright monomeric red fluorescent protein for cellular imaging. Nat Methods 14, 53–56.
5. Blanchoin, L, Boujemaa-Paterski, R, Sykes, C, and Plastino, J (2014). Actin dynamics, architecture, and mechanics in cell motility. Physiol Rev 94, 235–263.
6. Bolino, A et al. (2000). Charcot-Marie-Tooth type 4B is caused by mutations in the gene encoding myotubularin-related protein-2. Nat Genet 25, 17–19.
7. Cadart, C, Zlotek-Zlotkiewicz, E, Venkova, L, Thouvenin, O, Racine, V, Le Berre, M, Monnier, S, and Piel, M (2017). Fluorescence eXclusion measurement of volume in live cells. Methods Cell Biol 139, 103–120.
8. Castoldi, M, and Popov, AV (2003). Purification of brain tubulin through two cycles of polymerization-depolymerization in a high-molarity buffer. Protein Expr Purif 32, 83–88.
9. Chandra, M et al. (2019). Classification of the human phox homology (PX) domains based on their phosphoinositide binding specificities. Nat Commun 10, 1528.
10. Chang, F, Drubin, D, and Nurse, P (1997). Cdc12p, a protein required for cytokinesis in fission yeast, is a component of the cell division ring and interacts with profilin. J Cell Biol 137, 169–182.
11. Christ, KV, Williamson, KB, Masters, KS, and Turner, KT (2010). Measurement of single-cell adhesion strength using a microfluidic assay. Biomed Microdevices 12, 443–455.
12. Consolati, T et al. (2020). Microtubule nucleation properties of single human γTuRCs explained by their cryo-EM structure. Dev Cell 53, 603-617.e8.
13. Cooper, JA, Blum, JD, and Pollard, TD (1984). Acanthamoeba castellanii capping protein: properties, mechanism of action, immunologic cross-reactivity, and localization. J Cell Biol 99, 217–225.
14. Courtemanche, N, and Pollard, TD (2013). Interaction of profilin with the barbed end of actin filaments. Biochemistry 52, 6456–6466.
15. Davey, RJ, and Moens, PD (2020). Profilin: many facets of a small protein. Biophys Rev 12, 827–849.
16. De Craene, J-O, Bertazzi, D, Bär, S, and Friant, S (2017). Phosphoinositides, major actors in membrane trafficking and lipid signaling pathways. Intl J Mol Sci 18, 634.
17. DeCaprio, J, and Kohl, TO (2020). Differential detergent lysis of cellular fractions for immunoprecipitation. Cold Spring Harb Protoc 2, 098582.
18. Di Nardo, A, Gareus, R, Kwiatkowski, D, and Witke, W (2000). Alternative splicing of the mouse profilin II gene generates functionally different profilin isoforms. J Cell Sci 113, 3795–3803.

19. Ding, Z, Bae, YH, and Roy, P (2012). Molecular insights on context-specific role of profilin-1 in cell migration. Cell Adh Migr 6, 442–449.
20. Dong, J, Radau, B, Otto, A, Müller, E-C, Lindschau, C, and Westermann, P (2000). Profilin I attached to the Golgi is required for the formation of constitutive transport vesicles at the trans-Golgi network. Biochim Biophys Acta Mol Cell Res 2, 253–260.
21. Eads, JC, Mahoney, NM, Vorobiev, S, Bresnick, AR, Wen, K-K, Rubenstein, PA, Haarer, BK, and Almo, SC (1998). Structure determination and characterization of Saccharomyces cerevisiae profilin. Biochemistry 37, 11171–11181.
22. Evangelista, M, Blundell, K, Longtine, MS, Chow, CJ, Adames, N, Pringle, JR, Peter, M, and Boone, C (1997). Bni1p, a yeast formin linking cdc42p and the actin cytoskeleton during polarized morphogenesis. Science 276, 118–122.
23. Evangelista, M, Pruyne, D, Amberg, DC, Boone, C, and Bretscher, A (2002). Formins direct Arp2/3-independent actin filament assembly to polarize cell growth in yeast. Nat Cell Biol 4, 260–269.
24. Ezezika, OC, Younger, NS, Lu, J, Kaiser, DA, Corbin, ZA, Nolen, BJ, Kovar, DR, and Pollard, TD (2009). Incompatibility with formin Cdc12p prevents human profilin from substituting for fission yeast profilin: insights from crystal structures of fission yeast profilin. J Biol Chem 284, 2088–2097.
25. Ferron, F, Rebowski, G, Lee, SH, and Dominguez, R (2007). Structural basis for the recruitment of profilin-actin complexes during filament elongation by Ena/VASP. EMBO J 26, 4597–4606.
26. Figley, MD, Bieri, G, Kolaitis, R-M, Taylor, JP, and Gitler, AD (2014). Profilin 1 associates with stress granules and ALS-linked mutations alter stress granule dynamics. J Neurosci 34, 8083–8097.
27. Funk, J, Merino, F, Venkova, L, Heydenreich, L, Kierfeld, J, Vargas, P, Raunser, S, Piel, M, and Bieling, P (2019). Profilin and formin constitute a pacemaker system for robust actin filament growth. Elife 8, e50963.
28. Gertler, FB, Niebuhr, K, Reinhard, M, Wehland, J, and Soriano, P (1996). Mena, a relative of VASP and Drosophila Enabled, is implicated in the control of microfilament dynamics. Cell 87, 227–239.
29. Goldschmidt-Clermont, PJ, Furman, MI, Wachsstock, D, Safer, D, Nachmias, VT, and Pollard, TD (1992). The control of actin nucleotide exchange by thymosin beta 4 and profilin. A potential regulatory mechanism for actin polymerization in cells. Mol Biol Cell 3, 1015–1024.
30. Goldschmidt-Clermont, PJ, Machesky, LM, Baldassare, JJ, and Pollard, TD (1990). The actin-binding protein profilin binds to PIP2 and inhibits its hydrolysis by phospholipase C. Science 247, 1575–1578.
31. Grenklo, S, Johansson, T, Bertilson, L, and Karlsson, R (2004). Anti-actin antibodies generated against profilin:actin distinguish between non-filamentous and filamentous actin, and label cultured cells in a dotted pattern. Eur J Cell Biol 83, 413–423.
32. Groen, AC, Ngyuen, PA, Field, CM, Ishihara, K, and Mitchison, TJ (2014). Glycogen-supplemented mitotic cytosol for analyzing Xenopus egg microtubule organization. Meth Enzymol 540, 417–433.
33. Hartwig, JH, Chambers, KA, Hopcia, KL, and Kwiatkowski, DJ (1989). Association of profilin with filament-free regions of human leukocyte and platelet membranes and reversible membrane binding during platelet activation. J Cell Biol 109, 1571–1579.
34. Hasegawa, J, Strunk, BS, and Weisman, LS (2017). PI5P and PI(3,5)P_2: minor, but essential phosphoinositides. Cell Struct Funct 42, 49–60.
35. Henty-Ridilla, JL, and Goode, BL (2015). Global resource distribution: allocation of actin building blocks by profilin. Dev Cell 32, 5–6.
36. Henty-Ridilla, JL, Juanes, MA, and Goode, BL (2017). Profilin directly promotes microtubule growth through residues mutated in amyotrophic lateral sclerosis. Curr Biol 27, 3535-3543.e4.
37. Henty-Ridilla, JL, Rankova, A, Eskin, JA, Kenny, K, and Goode, BL (2016). Accelerated actin filament polymerization from microtubule plus ends. Science 352, 1004-1009.
38. Higgs, HN, and Pollard, TD (1999). Regulation of actin polymerization by Arp2/3 complex and WASp/scar proteins. J Biol Chem 274, 32531–32534.
39. Hong, NH, Qi, A, and Weaver, AM (2015). PI(3,5)P2 controls endosomal branched actin dynamics by regulating cortactin–actin interactions. J Cell Biol 210, 753–769.
40. Ikonomov, OC, Sbrissa, D, and Shisheva, A (2006). Localized PtdIns 3,5-P2 synthesis to regulate early endosome dynamics and fusion. Am J Physiol Cell Physiol 291, C393-404.
41. Isogai, T, van der Kammen, R, and Innocenti, M (2015). SMIFH2 has effects on formins and p53 that perturb the cell cytoskeleton. Sci Rep 5, 9802.
42. Janmey, PA, Bucki, R, and Radhakrishnan, R (2018). Regulation of actin assembly by PI(4,5)P2 and other inositol phospholipids: an update on possible mechanisms. Biochem Biophys Res Commun 506, 307–314.
43. Jean, C, Rieger, K, Blanchoin, L, Carlier, MF, Lenfant, M, and Pantaloni, D (1994). Interaction of G-actin with thymosin beta 4 and its variants thymosin beta 9 and thymosin beta met9. J Muscle Res Cell Motil 15, 278–286.
44. Jégou, A, Niedermayer, T, Orbán, J, Didry, D, Lipowsky, R, Carlier, M-F, and Romet-Lemonne, G (2011). Individual actin filaments in a microfluidic flow reveal the mechanism of ATP hydrolysis and give insight into the properties of profilin. PLoS Biol 9, e1001161.
45. Kaiser, DA, Vinson, VK, Murphy, DB, and Pollard, TD (1999). Profilin is predominantly associated with monomeric actin in Acanthamoeba. J Cell Sci 112, 3779–3790.
46. Karlsson, R, and Dráber, P (2021). Profilin-A master coordinator of actin and microtubule organization in mammalian cells. J Cell Physiol 236, 7256–7265.

47. Koestler, SA, Rottner, K, Lai, F, Block, J, Vinzenz, M, and Small, JV (2009). F- and G-actin concentrations in lamellipodia of moving cells. PLoS ONE 4, e4810.
48. Kovar, DR, Harris, ES, Mahaffy, R, Higgs, HN, and Pollard, TD (2006). Control of the assembly of ATP- and ADP-actin by formins and profilin. Cell 124, 423–435.
49. Kremers, G-J, Hazelwood, KL, Murphy, CS, Davidson, MW, and Piston, DW (2009). Photoconversion in orange and red fluorescent proteins. Nat Methods 6, 355–358.
50. Krishnan, K, and Moens, PDJ (2009). Structure and functions of profilins. Biophys Rev 1, 71–81.
51. Lambrechts, A, Jonckheere, V, Dewitte, D, Vandekerckhove, J, and Ampe, C (2002). Mutational analysis of human profilin I reveals a second $PI_{(4,5)}$-P2 binding site neighbouring the poly(L-proline) binding site. BMC Biochem 3, 12.
52. Lassing, I, and Lindberg, U (1985). Specific interaction between phosphatidylinositol 4,5-bisphosphate and profilactin. Nature 314, 472–474.
53. Lees, JA, Li, P, Kumar, N, Weisman, LS, and Reinisch, KM (2020). Insights into lysosomal PI(3,5)P2 homeostasis from a structural-biochemical analysis of the PIKfyve lipid kinase complex. Mol Cell 80, 736-743.e4.
54. Mammoto, A, Sasaki, T, Asakura, T, Hotta, I, Imamura, H, Takahashi, K, Matsuura, Y, Shirao, T, and Takai, Y (1998). Interactions of drebrin and gephyrin with profilin. Biochem Biophys Res Commun 243, 86–89.
55. Martys, JL, Wjasow, C, Gangi, DM, Kielian, MC, McGraw, TE, and Backer, JM (1996). Wortmannin-sensitive trafficking pathways in Chinese hamster ovary cells. Differential effects on endocytosis and lysosomal sorting. J Biol Chem 271, 10953–10962.
56. Michaelsen-Preusse, K, Zessin, S, Grigoryan, G, Scharkowski, F, Feuge, J, Remus, A, and Korte, M (2016). Neuronal profilins in health and disease: Relevance for spine plasticity and Fragile X syndrome. Proc Natl Acad Sci USA 113, 3365–3370.
57. Michell, RH, Heath, VL, Lemmon, MA, and Dove, SK (2006). Phosphatidylinositol 3,5-bisphosphate: metabolism and cellular functions. Trends Biochem Sci 31, 52–63.
58. Miki, H, Suetsugu, S, and Takenawa, T (1998). WAVE, a novel WASP-family protein involved in actin reorganization induced by Rac. EMBO J 17, 6932–6941.
59. Miller, AL, and Bement, WM (2009). Regulation of cytokinesis by Rho GTPase flux. Nat Cell Biol 11, 71–77.
60. Moens, PDJ, and Coumans, JVF (2015). Profilin-1 mediated cell-cycle arrest: searching for drug targets. Cell Cycle 14, 3669–3670.
61. Nejedlá, M, Klebanovych, A, Sulimenko, V, Sulimenko, T, Dráberová, E, Dráber, P, and Karlsson, R (2021). The actin regulator profilin 1 is functionally associated with the mammalian centrosome. Life Sci Alliance 4, e202000655.
62. Nejedla, M, Li, Z, Masser, AE, Biancospino, M, Spiess, M, Mackowiak, SD, Friedländer, MR, and Karlsson, R (2017). A fluorophore fusion construct of human profilin I with non-compromised poly(L-proline) binding capacity suitable for Imaging. J Mol Biol 429, 964–976.
63. Nejedla, M, Sadi, S, Sulimenko, V, de Almeida, FN, Blom, H, Draber, P, Aspenström, P, and Karlsson, R (2016). Profilin connects actin assembly with microtubule dynamics. Mol Biol Cell 27, 2381–2393.
64. Niggli, V (2005). Regulation of protein activities by phosphoinositide phosphates. Annu Rev Cell Dev Biol 21, 57–79.
65. Nishimura, Y, Shi, S, Zhang, F, Liu, R, Takagi, Y, Bershadsky, AD, Viasnoff, V, and Sellers, JR (2021). The formin inhibitor SMIFH2 inhibits members of the myosin superfamily. J Cell Sci 134, jcs253708.
66. Oliinyk, OS, Shemetov, AA, Pletnev, S, Shcherbakova, DM, and Verkhusha, VV (2019). Smallest near-infrared fluorescent protein evolved from cyanobacteriochrome as versatile tag for spectral multiplexing. Nat Commun 10, 279.
67. Pernier, J, Shekhar, S, Jegou, A, Guichard, B, and Carlier, M-F (2016). Profilin interaction with actin filament barbed end controls dynamic instability, capping, branching, and motility. Dev Cell 36, 201–214.
68. Pimm, ML, and Henty-Ridilla, JL (2021). New twists in actin-microtubule interactions. Mol Biol Cell 32, 211–217.
69. Pimm, ML, Hotaling, J, and Henty-Ridilla, JL (2020). Profilin choreographs actin and microtubules in cells and cancer. Int Rev Cell Mol Biol. 355, 155-204.
70. Pinto-Costa, R, and Sousa, MM (2019). Profilin as a dual regulator of actin and microtubule dynamics. Cytoskeleton 3-4, 76-83.
71. Pollard, TD, Blanchoin, L, and Mullins, RD (2000). Molecular mechanisms controlling actin filament dynamics in nonmuscle cells. Annu Rev Biophys Biomol Struct 29, 545–576.
72. Popov, AV, Severin, F, and Karsenti, E (2002). XMAP215 is required for the microtubule-nucleating activity of centrosomes. Curr Biol 12, 1326–1330.
73. Reinhard, M, Giehl, K, Abel, K, Haffner, C, Jarchau, T, Hoppe, V, Jockusch, BM, and Walter, U (1995). The proline-rich focal adhesion and microfilament protein VASP is a ligand for profilins. EMBO J 14, 1583–1589.
74. Rodal, AA, Manning, AL, Goode, BL, and Drubin, DG (2003). Negative regulation of yeast WASp by two SH3 domain-containing proteins. Curr Biol 13, 1000–1008.
75. Rotty, JD, Wu, C, Haynes, EM, Suarez, C, Winkelman, JD, Johnson, HE, Haugh, JM, Kovar, DR, and Bear, JE (2015). Profilin-1 serves as a gatekeeper for actin assembly by Arp2/3-dependent and -independent pathways. Dev Cell 32, 54–67.
76. Schindelin, J et al. (2012). Fiji: an open-source platform for biological-image analysis. Nat Methods 9, 676–682.

77. Schutt, CE, Myslik, JC, Rozycki, MD, Goonesekere, NCW, and Lindberg, U (1993). The structure of crystalline profilin-beta-actin. Nature 365, 810–816.
78. Shaner, NC, Lin, MZ, McKeown, MR, Steinbach, PA, Hazelwood, KL, Davidson, MW, and Tsien, RY (2008). Improving the photostability of bright monomeric orange and red fluorescent proteins. Nat Methods 5, 545–551.
79. Skare, P, and Karlsson, R (2002). Evidence for two interaction regions for phosphatidylinositol(4,5)-bisphosphate on mammalian profilin I. FEBS Lett 522, 119–124.
80. Skruber, K, Read, T-A, and Vitriol, EA (2018). Reconsidering an active role for G-actin in cytoskeletal regulation. J Cell Sci 131, jcs203760.
81. Skruber, K, Warp, PV, Shklyarov, R, Thomas, JD, Swanson, MS, Henty-Ridilla, JL, Read, T-A, and Vitriol, EA (2020). Arp2/3 and mena/VASP require profilin 1 for actin network assembly at the leading dge. Curr Biol 30, 2651-2664.e5.
82. Smith, BA, Padrick, SB, Doolittle, LK, Daugherty-Clarke, K, Corrêa, IR, Xu, M-Q, Goode, BL, Rosen, MK, and Gelles, J (2013). Three-color single molecule imaging shows WASP detachment from Arp2/3 complex triggers actin filament branch formation. Elife 2, e01008.
83. Spudich, JA, and Watt, S (1971). The regulation of rabbit skeletal muscle contraction. I. Biochemical studies of the interaction of the tropomyosin-troponin complex with actin and the proteolytic fragments of myosin. J Biol Chem 246, 4866–4871.
84. Suarez, C, Carroll, RT, Burke, TA, Christensen, JR, Bestul, AJ, Sees, JA, James, ML, Sirotkin, V, and Kovar, DR (2015). Profilin regulates F-actin network homeostasis by favoring formin over Arp2/3 complex. Dev Cell 32, 43–53.
85. Suarez, C, and Kovar, DR (2016). Internetwork competition for monomers governs actin cytoskeleton organization. Nat Rev Mol Cell Biol 12, 799–810.
86. Suetsugu, S, Miki, H, and Takenawa, T (1998). The essential role of profilin in the assembly of actin for microspike formation. EMBO J 17, 6516–6526.
87. Sun, T, Li, S, and Ren, H (2013). Profilin as a regulator of the membrane-actin cytoskeleton interface in plant cells. Front Plant Sci 4, 512.
88. Tarachandani, A, and Wang, YL (1996). Site-directed mutagenesis enabled preparation of a functional fluorescent analog of profilin: biochemical characterization and localization in living cells. Cell Motil Cytoskeleton 34, 313–323.
89. Vidali, L, and Hepler, PK (1997). Characterization and localization of profilin in pollen grains and tubes of Lilium longiflorum. Cell Motil Cytoskeleton 36, 323–338.
90. Vinson, VK, De La Cruz, EM, Higgs, HN, and Pollard, TD (1998). Interactions of Acanthamoeba profilin with actin and nucleotides bound to actin. Biochemistry 37, 10871–10880.
91. Wallroth, A, and Haucke, V (2018). Phosphoinositide conversion in endocytosis and the endolysosomal system. J Biol Chem 293, 1526–1535.
92. Watanabe, N, and Mitchison, TJ (2002). Single-molecule speckle analysis of actin filament turnover in lamellipodia. Science 295, 1083–1086.
93. Wen, K-K, McKane, M, Houtman, JCD, and Rubenstein, PA (2008). Control of the ability of profilin to bind and facilitate nucleotide exchange from G-actin. J Biol Chem 283, 9444–9453.
94. Witke, W, Podtelejnikov, AV, Di Nardo, A, Sutherland, JD, Gurniak, CB, Dotti, C, and Mann, M (1998). In mouse brain profilin I and profilin II associate with regulators of the endocytic pathway and actin assembly. EMBO J 17, 967–976.
95. Witke, W, Sutherland, JD, Sharpe, A, Arai, M, and Kwiatkowski, DJ (2001). Profilin I is essential for cell survival and cell division in early mouse development. Proc Natl Acad Sci USA 98, 3832–3836.
96. Wittenmayer, N, Rothkegel, M, Jockusch, BM, and Schlüter, K (2000). Functional characterization of green fluorescent protein-profilin fusion proteins: GFP-profilin fusion proteins. Eur J Biochem 267, 5247–5256.
97. Wu, C-H et al. (2012). Mutations in the profilin 1 gene cause familial amyotrophic lateral sclerosis. Nature 488, 499–503.
98. Xue, B, Leyrat, C, Grimes, JM, and Robinson, RC (2014). Structural basis of thymosin-β4/profilin exchange leading to actin filament polymerization. Proc Natl Acad Sci USA 111, E4596-4605.
99. Zhu, C et al. (2021). Cancer-associated exportin-6 upregulation inhibits the transcriptionally repressive and anticancer effects of nuclear profilin-1. Cell Rep 34, 108749.
100. Zweifel, ME, and Courtemanche, N (2020). Competition for delivery of profilin-actin to barbed ends limits the rate of formin-mediated actin filament elongation. J Biol Chem. 295, 4513-4525.

Supplemental Figure Legends

Figure S1. Full-blots associated with tagged profilin binding phosphoinositide (PIP)-lipids. **(A)** Western blot of supernatants and pellets from liposome pelleting assays containing 1 μM profilin in absence (control) or presence of 0.33 mM of either phosphatidylinositol 3,5-bisphoshate ($PI(3,5)P_2$) or phosphatidylinositol 4,5-bisphoshate ($PI(4,5)P_2$) lipids. **(B)** Western blot of supernatants and pellets from liposome pelleting assays containing 1 μM mApple-profilin in absence (control) or presence of 0.33 mM of $PI(3,5)P_2$ or $PI(4,5)P_2$. Profilin-1 B 10 was used as a primary antibody (1:5,000 dilution; SantaCruz 137235) and goat anti-mouse 926-32210 was used as the secondary antibody (1:10,000 dilution; LI-COR Biosciences).

Figure S2. Untagged profilin is unsuitable for conventional anisotropy assays. Fluorescence anisotropy measurement of 10 nM OG-actin mixed with increasing concentrations of unlabeled profilin. Untagged- or unlabeled profilin is insufficient to elicit a change in anisotropy in our system (n = 1).

Figure S3. Localization of mApple-profilin with actin filaments in vitro. **(A)** Images from a multicolor TIRF movie of 1 μM actin monomers (10% Alexa-647-labeled; 0.6 nM biotin-actin) (cyan) polymerizing in the presence of 3 μM mApple-profilin-1 (pink). Tagged-profilin suppresses actin filament polymerization and rarely associates with actin filaments (one example is shown in the white box). Scale bar, 20 μm. **(B)** Zoomed in view of box in (A) showing the single observed example of mApple-profilin localized to the growing end of an actin filament. Scale bar, 10 μm. **(C)** Quantification of mApple-profilin association with actin filaments. All actin filaments from movies obtained (n = 3) were assessed for colocalization between mApple-profilin molecules with any portion of actin filaments from TIRF reactions as (A).

Figure S4. Full views of the effects of mApple-profilin on formin-mediated actin assembly. **(A)** Full views of montages of formin-mediated actin polymerization. Reactions contain 1 μM actin (10% Alexa-647-labeled; 0.6 nM biotin-actin) and 25 nM mDia1(FH1-C) and 5 μM profilin or 5 μM mApple-profilin. White box indicates the view presented in Figure 4B. Only the actin-wavelength (647 nm) is shown. **(B)** Full view of a multi-color time lapse TIRF montage. Reaction contains 1 μM actin (10% Alexa-647-labeled; 0.6 nM biotin-actin), 25 nM mDia1(FH1-C) and 5 μM mApple-profilin. The actin (647 nm) and mApple (561 nm) wavelengths are shown individually and merged. Scale bars, 20 μm.

Figure S5. Additional views of the effects of tagged profilin on microtubule dynamics. **(A)** Full views of montages displaying the effects of profilin on microtubule dynamics. Reactions contain 647-biotinylated-GMP-CCP microtubule seeds (not shown), 10 μM free tubulin (5% HiLyte488) and 5 μM profilin-1 (untagged) or 5 μM mApple-profilin-1. Black box indicates the view presented in Figure 5A. **(B)** Full view of a multi-color time lapse TIRF montage. Reaction contains 10 μM free tubulin (5% HiLyte488) and 5 μM mApple-profilin-1. Black box indicates the view presented in Figure 5H. Scale bars, 20 μm. **(C)** Montage of a single-microtubule from reactions as in (Figure 5H) showing each wavelength (and merge) of the view presented in Figure 5J. + and - indicate the microtubule polarity. Scale bar, 10 μm.

Figure S6. Full-blots used to determine profilin levels in Neuroblastoma-2a (N2a) cells. Full blots confirming CRISPR knockout and rescue of profilin-1 with either mAp-PFN1 or Halo-PFN1 constructs. N2a cell extracts were prepared from wild-type N2a ($PFN1^{(+/+)}$), profilin knockout ($PFN1^{(-/-)}$), or profilin knockout cells 24 h after transfection with a tag-less rescue construct, mAp-PFN1, or Halo-PFN1. **(A)** Blots were probed with Profilin-1 B 10 primary (1:3,500 dilution; SantaCruz 137235) and goat anti-mouse 926-32210 secondary (1:5,000 dilution; LiCor Biosciences) antibodies and also **(B)** α-tubulin primary (1:10,000; Abcam 18251) and donkey anti-rabbit secondary (1:20,000; 926-68073). **(C)** Coomassie stained membrane from (A) is shown as a loading control. **(D)** View of a full representative blot that was used to determine the concentration of endogenous profilin-1 in N2a cells. Blot was probed as in (A) for profilin-1 (D) or α-tubulin **(E)** and later **(F)** Coomassie stained to compare to known quantities of purified mApple-profilin (43 kDa) or untagged profilin (15 kDa). **(G)** Super resolution confocal imaging of wild-type (endogenous; blue), profilin knockout ($PFN1^{(-/-)}$; cyan), or $PFN1^{(-/-)}$ transfected with mApple-PFN1 (pink) cells plated on Y micropatterns. N2a cells are shown individually and as an overlay aligned by the micropattern. Cells were imaged 24 h after transfection. At least 10 cells were analyzed per coverslip and n = 3 coverslips were analyzed per condition. **(H)** Quantification of cell morphology, calculated as a ratio of cell area to endogenous control cells from images similar to (G and Figures 6F-I). $PFN1^{(-/-)}$ cells displayed significantly aberrant morphology, cells rescued with mApple-profilin plasmid were not significantly different compared to endogenous controls ($PFN1^{(+/+)}$). Error bars indicate SE across independent experiments (different coverslips). Significant differences by one-way ANOVA with Bartlett's correction for variance: ns, not significantly different from endogenous $PFN1^{(+/+)}$ control; a, compared with control ($p < 0.05$). Scale bars, 10 μm.

Figure S7. Live cell localization of constructs of Halo-profilin-1. **(A)** Maximum intensity Z-projections of SoRa spinning disk confocal imaged profilin-$1^{(+/+)}$ cells (N2a) transiently expressing GFP-actin (black), ensconsin microtubule binding domain (EMTB)-2×mCherry (microtubules; magenta), and JF-646 labeled Halo-profilin-1 or JF-646 Halo-R88E (light blue). 10 nM Halo-ligand was used to visualize profilin constructs. **(B)** The bottom 2 μm of Z-projections from cells in (A) were scored for

association (pixel overlap) with microtubules (faint or bright). **(C)** full view of N2A cells as in (A) showing the placement of lines for kymographs in Figure 7D. Scale bars, 10 µm.

Supplemental Movie 1. TIRF microscopy comparing the effects of untagged profilin-1 or mApple-profilin-1 on actin assembly. Reaction components: 1 µM actin monomers (20% Oregon Green (OG)-labeled; 0.6 nM biotin-actin). Variable components 3 µM profilin-1 (untagged) or 3 µM mApple-profilin-1. Only the actin wavelength (488 nm) is shown. Video playback is 10 frames per s. Scale bars, 10 µm.

Supplemental Movie 2. Multi-color TIRF microscopy of mApple-profilin on actin assembly. Reaction components: 1 µM actin monomers (20% OG-labeled; 0.6 nM biotin-actin) (cyan) and 3 µM mApple-profilin-1 (pink). The actin (488 nm) and mApple (561 nm) wavelengths are shown individually and merged. White box corresponds to montage inset from Figure S3B. Video playback is 10 frames per s. Scale bars, 10 µm.

Supplemental Movie 3. TIRF microscopy comparing the effects of untagged profilin-1 or mApple-profilin-1 on formin-mediated actin filament assembly. Reaction components: 1 µM actin monomers (10% Alexa-647-labeled; 0.6 nM biotin-actin). Variable components 5 µM profilin-1 (untagged) or 5 µM mApple-profilin-1. Only the actin wavelength (647 nm) is shown. White box corresponds to montage from Figures 4B and S4A. Video playback is 10 frames per s. Scale bars, 10 µm.

Supplemental Movie 4. Multi-color TIRF microscopy of mApple-profilin on formin-mediated actin filament assembly. Reaction components: 1 µM actin monomers (10% Alexa-647-labeled; 0.6 nM biotin-actin) (cyan) and 5 µM mApple-profilin-1 (pink). The actin (647 nm) and mApple (561 nm) wavelengths are shown individually and merged. Video playback is 10 frames per s. Scale bars, 10 µm.

Supplemental Movie 5. TIRF microscopy comparing the effects of untagged profilin-1 or mApple-profilin-1 on microtubule dynamics. Reaction components: 647-biotinylated-GMP-CCP microtubule seeds (not shown), 10 µM free tubulin (5% HiLyte488). Variable components 5 µM profilin-1 (untagged) or 5 µM mApple-profilin-1. Only the polymerizing microtubule wavelength (488 nm) is shown. Black box corresponds to montage inset from Figure 5A Video playback is 10 frames per s. Scale bars, 20 µm.

Supplemental Movie 6. Multi-color TIRF microscopy of mApple-profilin on microtubule dynamics. Reaction components: 647-biotinylated-GMP-CCP microtubule seeds (not shown), 10 µM free tubulin (5% HiLyte488) (black) and 5 µM mApple-profilin-1 (pink). The polymerizing microtubule (488 nm) and mApple-profilin wavelengths (561 nm) are shown individually and merged. Box corresponds to montage inset from Figure 5H. Video playback is 10 frames per s. Scale bars, 20 µm.

Supplemental Movie 7. Profilin transiently binds and associates with the microtubule lattice. Reaction components: 647-biotinylated-GMP-CCP microtubule seeds (not shown), 10 µM free tubulin (5%HiLyte488) (black) and 5 µM mApple-profilin-1 (pink). The polymerizing microtubule (488 nm) and mApple-profilin wavelengths (561 nm) are shown individually and merged. + and - indicate the microtubule polarity. Video playback is 10 frames per s. Scale bar, 10 µm.

Supplemental Movie 8. Profilin dynamics in live-cells. SoRa super resolution spinning disk confocal 4D movie of the bottom 2 µm of N2a cells transiently expressing GFP-actin (cyan), ensconsin microtubule binding domain (EMTB)-2×mCherry (microtubules; yellow), and JF-646 labeled Halo-profilin-1 constructs (magenta). 10 nM Halo-ligand was used to visualize a subset of total cellular profilin. Video playback is 10 frames per s. Total elapsed time is 3 min. Scale bar, 10 µm.